

PWO Crystal Measurements and Simulation Studies of $\bar{\Lambda}$ Hyperon Polarisation for PANDA

Licenciate Thesis
Sophie Grape

Department for Physics and Astronomy, Uppsala University

January 2008

Abstract

The Gesellschaft für Schwerionenforschung (GSI) facility in Darmstadt, Germany, will be upgraded to accommodate a new generation of physics experiments. The future accelerator facility will be called FAIR and one of the experiments at the site will be PANDA, which aims at performing hadron physics investigations by colliding anti-protons with protons. The licentiate thesis consists of three sections related to PANDA. The first contains energy resolution studies of PbWO₄ crystals, the second light yield uniformity studies of PbWO₄ crystals and the third reconstruction of the $\bar{\Lambda}$ -polarisation in the PANDA experiment.

Two measurements of the energy resolution were performed at MAX-Lab in Lund, Sweden, with an array of 3×3 PbWO₄ crystals using a tagged photon beam with energies between 19 and 56 MeV. For the April measurement, the crystals were cooled down to -15 °C and for the September measurement down to -25 °C. The measured relative energy resolution, σ/E , is decreasing from approximately 12% at 20 MeV to 7% at 55 MeV. In the standard energy resolution expression $\sigma/E = a/\sqrt{E} \oplus b/E \oplus c$, the three parameters a , b , c seem to be strongly correlated and thus difficult to determine independently over this relative small energy range. The value of a was therefore fixed to that one would expect from Poisson statistics of the light collection yield (50 phe/MeV) and the results from fits were $\sigma/E = 0.45\%/\sqrt{E_{GeV}} \oplus 0.18\%/E_{GeV} \oplus 8.63\%$ and $\sigma/E = 0.45\%/\sqrt{E_{GeV}} \oplus 0.21\%/E_{GeV} \oplus 6.12\%$ for the April and September measurements, respectively. The data from the September measurement was also combined with previous data from MAMI for higher energies, ranging from approximately 64 to 715 MeV. The global fit over the whole range of energies gave an energy resolution expression of $\sigma/E = 1.6\%/\sqrt{E_{GeV}} \oplus 0.095\%/E_{GeV} \oplus 2.1\%$.

Light yield uniformity studies of five PbWO₄ crystals, three tapered and two non-tapered ones, have also been performed. The tapered crystals delivered a light output which increased with increasing distance from the Photo Multiplier Tube (PM tube). Black tape was put on different sides of one tapered crystals, far from the PM tube to try to get a more constant uniformity profile. It was seen that the light output profile depends on the position of the tape. Generally, the steep increase in light output at large distances from the PM tube could be damped.

The third part of the thesis concerns the reconstruction of the $\bar{\Lambda}$ polarisation in the reaction $\bar{p}p \rightarrow \bar{\Lambda}\Lambda$. Events were generated using a modified generator from the PS185 experiment at LEAR. With a 100% polarisation perpendicular to the scattering plane, a polarisation of $(99 \pm 1.8)\%$ was reconstructed. Slight non-zero polarisations along the axis determined by the outgoing hyperon as well as the axis in the scattering plane, were also reconstructed. These were

$(4.1 \pm 2.1)\%$ and $(2.6 \pm 2.0)\%$ respectively. From this investigation it was shown that the detector efficiency was not homogeneous and that slow pions are difficult to reconstruct.

Contents

1	Introduction	7
2	Theoretical Background	8
2.1	Fundamental Particles	8
2.2	Interactions	9
2.3	Configurations and Symmetries	9
2.4	Physics of Interest to the PANDA Collaboration	10
2.4.1	Charmonium Spectroscopy	10
2.4.2	Hybrids and Glueballs	11
2.4.3	Hyperons	11
2.4.4	Hypernuclei	11
3	FAIR and the PANDA Detector	13
3.1	The GSI and FAIR Facilities	13
3.2	The PANDA Detector	14
3.2.1	The Target Spectrometer	15
3.2.2	The Forward Spectrometer	19
4	Energy Measurements with Crystals	21
4.1	Particle Interactions in Scintillators	21
4.1.1	Photon Interactions with Matter	21
4.1.2	Electron Interactions with Matter	23
4.2	Energy Resolution	24
4.2.1	Energy Resolution for PANDA	25
4.3	PbWO ₄ Scintillator Characteristics	27
5	Energy Resolution Measurements with PANDA Crystals	29
5.1	The Tagged Photon Facility at MAX-Lab in Lund	29
5.2	Measurement Set-up	31
5.3	The Read-Out Electronics	33
5.4	Analysis	34
5.5	Relative Calibration	35
5.6	Results from Measurements below 60 MeV, April 2007	37
5.7	Results from Measurements below 60 MeV, September 2007	42
5.8	Comparison with Previous Data	45
5.9	Discussion and Conclusion from the Energy Resolution Measurements	49

6	Light Yield Uniformity Tests of PANDA Crystals	52
6.1	Set-Up for Uniformity Tests	52
6.2	Statistics	54
6.3	Analysis	55
6.4	Results	55
6.5	Light Yield Uniformity Improvements	56
6.6	Discussion and Conclusions from the Uniformity Results	59
7	Simulation Studies	62
7.1	Introduction	62
7.2	About the Λ State	62
7.3	The Coordinate System	63
7.4	The Angular Distributions of the Λ	63
7.5	Λ Polarisation	65
7.5.1	How to Reconstruct the Λ Polarisation	65
7.6	The PANDA Software Frameworks	66
7.7	Reconstruction	67
7.7.1	Generation of Particles	67
7.7.2	Angular Distribution	67
7.7.3	Detector and Detection Efficiency	68
7.7.4	The Polarisation	74
7.7.5	Momentum and Vertex Reconstruction	77
7.8	Conclusions from the Simulation Results	83
8	Conclusion and Outlook	85
8.1	Conclusion	85
8.2	Outlook	86

Chapter 1

Introduction

The PANDA acronym stands for antiProton ANnihilation DArmstadt and it represents an international physics collaboration consisting of more than 420 collaborators from 55 institutions in 17 countries. The detector was planned in the 1990's and is foreseen to start operating around year 2015. The main purpose of the PANDA detector is to do research with anti-protons and hadronic matter to gain better knowledge of the strong interaction.

The PANDA experiment will be carried out at FAIR, the Facility for Antiproton and Ion Research which will be built at the site of GSI, the Gesellschaft für Schwerionenforschung. The facility is located outside of Darmstadt in Germany. GSI was upgraded 15 years ago, allowing for a new heavy-ion accelerator. However, the future FAIR facility is more than an upgrade of GSI, it will allow for a whole new generation of medium energy physics experiments with anti-protons.

This licenciate thesis treats two topics of interest to the PANDA collaboration. The first concerns studies of interest to the electromagnetic calorimeter. It involves energy resolution measurements and light yield uniformity test for photons in PWO crystals. The second part involves simulations of the ability to correctly reconstruct $\bar{\Lambda}$ hyperons and their polarisation. The two topics will be joined together via the electromagnetic calorimeter in future studies. The light Λ state is, in many cases, the decay product of heavier hyperons that either decay radiatively (emitting photons) or into particles which decay into photons.

Chapter 2

Theoretical Background

The Standard Model contains the theory of the electroweak interaction and the strong interaction (Quantum Chromo Dynamics, QCD). It incorporates the 12 fundamental particles we know of, three of their interactions as well as the carriers of these.

2.1 Fundamental Particles

There are two groups of fundamental particles carrying half-integer spin (fermions): quarks and leptons. The quarks are of six different flavours and are called the up-, down-, strange-, charm-, bottom- and top quarks. They are organised into three generations, depending on their mass and electric charge. Each generation consists of one positively and one negatively charged quark and includes particles which are lighter than the ones in the following generation.

Generation	Name	Charge (e)	Mass [GeV/ c^2]	Spin
1	Up (u)	+2/3	0.0015-0.003	1/2
	Down (d)	-1/3	0.003-0.007	1/2
2	Charm (c)	+2/3	1.25±0.09	1/2
	Strange (s)	-1/3	0.95±0.25	1/2
3	Top (t)	+2/3	172-174	1/2
	Bottom (b)	-1/3	4.2-4.7	1/2

Table 2.1: The six quarks and some of their properties [1].

All quarks also carry the charge of the strong interaction which is called the colour charge. This charge comes in the varieties of red, green or blue. These charges solve the problem on how to separate identical fermions from each other according to the Pauli principle (which says that a fermion cannot be in the same quantum state as another fermion). If the colour charge did not exist, it would not be possible to separate the three s-quarks in the Ω^- -baryon or the u-quarks in Δ^{++} from each other.

Individual quarks have never been found freely, they are always found in colour neutral configurations with two other quarks or one anti-quark. This feature is called confinement. The quarks are building blocks for so-called

hadrons, strongly interacting particles, and they are divided into mesons and baryons. Mesons represent the quark-anti-quark ($q\bar{q}$) configurations and have integer spin, while baryons are made up of three quarks and carry half-integer spin. There might be other configurations as well, but these two possibilities represent what is experimentally established today.

The leptons form the second group of these fundamental particles. They are also grouped into three generations.

Generation	Name	Charge (e)	Mass [MeV/ c^2]	Spin
1	Electron (e^-)	-1	0.511	1/2
	Electron neutrino (ν_e)	0	$< 2 \cdot 10^{-6}$	1/2
2	Muon (μ^-)	-1	106.5	1/2
	Muon neutrino (ν_μ)	0	< 0.19	1/2
3	Tau (τ^-)	-1	1777	1/2
	Tau neutrino (ν_τ)	0	< 0.018	1/2

Table 2.2: The six leptons and some of their properties [1].

2.2 Interactions

There are four fundamental forces which govern the interactions in nature; the electromagnetic, the weak, the strong and the gravitational force. All but the last are incorporated into the Standard Model. The interactions are described by quantum field theory and their interactions are mediated by the quanta of the respective fields, the so-called gauge bosons. The gravitational force is much weaker than the other three forces and will not be considered here.

The electromagnetic force is mediated by the massless photon, making the range of the force infinite. This force keeps the electrons bound to the atomic nucleus and the atoms bound to other atoms in materials. Hadrons which decay with this type of interaction usually have life times of $10^{-16} - 10^{-21}$ s [2].

The weak force is mediated by the neutral Z boson and the flavour changing charged W^\pm bosons. Probably the most easily noticeable effect of this force is the radioactive decays where protons are transformed into neutrons or vice versa. Due to the heavy mass of these gauge bosons, the force only acts on small distances and the life times of decaying particles are typically $10^{-7} - 10^{-13}$ s [2].

The strong force is mediated by the massless gluons which carry both colour and anti-colour charge. At low energies it is useful to consider the hadronic degrees of freedom for the interaction instead of quarks and gluons. In this case the mediating particles are mesons, pions for short range interactions and omega for long range. The range of the strong force is about 10^{-15} m and the decay times are typically $10^{-22} - 10^{-24}$ s [2].

2.3 Configurations and Symmetries

There are certain rules that systems of quarks must obey. These rules are set by conservation laws of the so-called quantum numbers which characterise the system.

All interactions of the Standard Model conserve spin and angular momentum. The strong and electromagnetic interactions both conserve flavour, time reversal T, the charge conjugation quantum number C, the parity P and of course the combination of them (CP), while the weak interaction violates all of these symmetries (to some degree). CPT symmetry is the only symmetry obeyed by all three interactions.

Different states (particles) can be labelled using, for instance, the spectroscopic notation $n^{2S+1}L_J$ with n being the main quantum number, S the spin quantum number, L the relative angular momentum quantum number and J the total spin quantum number of the system. The total spin J is expressed as the sum of L and S , $\mathbf{L} + \mathbf{S}$.

Charge conjugation (C) is the operation where particles are replaced by their corresponding anti-particles in the same state. The C quantum number is given by [2]

$$C_{\text{boson}} = (-1)^L, \quad C_{\text{fermion}} = (-1)^{L+S}. \quad (2.1)$$

The parity P for a meson and a baryon are expressed as [2]

$$P_{\text{meson}} = (-1)^{L+1}, \quad P_{\text{baryon}} = (-1)^{L_{12}+L_3} \quad (2.2)$$

where L_{12} and L_3 are the internal angular momentum between two arbitrarily chosen quarks and the orbital angular momentum of the third quark about the center of mass of the pair.

In addition to the spectroscopic notation, one may add the quantum numbers J^{PC} of the configuration to more fully describe it.

2.4 Physics of Interest to the PANDA Collaboration

The PANDA experiment has many different physics objectives, mostly related to the strong interaction and some of them are mentioned below. The purpose of the PANDA hadron physics program is to study hadronic structures and hadronic interactions in the non-perturbative regime. New states will be searched for and possibilities for gluonic excitations such as hybrids and glue-balls will be investigated [4].

2.4.1 Charmonium Spectroscopy

Charmonium, the bound state of a charm quark and an anti-charm quark, is a very interesting configuration. The charm quark mass is relatively large, luckily heavy enough for non-relativistic calculations to be (barely) applicable [5]. In addition, the strong coupling constant α_s is fairly small for the system, ≈ 0.3 , which makes it possible to use perturbative calculations [5]. Charmonium states are also generally very narrow states, at least below the threshold of open charm production where the charmed quark pair must annihilate to create lighter quarks. Narrow states are easier to interpret, since the risk of having overlapping states is decreased and mixing effects between these states are generally small.

Charmonium studies started in e^+e^- collisions back in 1974. In these types

of collisions, the quantum numbers of the intermediate photon, $J^{PC}=1^{--}$, dictates that only charmonium states with these quantum numbers can be directly created. However, if anti-protons are collided with protons, a whole new world of possibilities opens up. The initial system can have any quantum numbers that are available to a system comprising a fermion and an anti-fermion. The final state quantum numbers are given by the gluon(s) and quarks coming from the initial state. This makes it possible to end up with a broad range of allowed J^{PC} quantum numbers. In the case of the created particle having a J^{PC} that is “forbidden” according to the rules for the naive quark model mentioned in section 2.3, they are labelled “exotic”[2]. No such particles have so far been firmly established.

2.4.2 Hybrids and Glueballs

Hybrid and glueball configurations are thought to exist in parallel to the conventional hadrons. A hybrid is a meson state where gluonic excitations are present together with quarks, while a glueball is a state entirely built up by glue [6].

There are observed states which do not fully seem to fit into the naive quark model, where all hadrons can be described with three quarks or one quark and an anti-quark. For charmonium, this is the case e.g. for the recently observed so-called X, Y and Z states [7]. Such states are candidates for being di-quarks, molecule states, exotic particles, hybrids or glueballs and the PANDA collaboration wishes to shed some light over this.

2.4.3 Hyperons

Hyperons are baryons with at least one s-quark. To conserve strangeness, they are always produced in a process where pairs of $\bar{s}s$ quarks are created.

The proton and the Λ are assumed to have a di-quark-quark structure in the constituent quark model. The di-quark, being the ud -pair, is in an isospin and spin zero state and one may regard the di-quarks as spectators in the reaction $\bar{p}p \rightarrow \bar{\Lambda}\Lambda$. This is important, since this implicates that the observables more directly reflect the dynamics of the underlying $\bar{u}u \rightarrow \bar{s}s$ -process [8].

Studies have shown that $\bar{\Lambda}\Lambda$ hyperon pairs are practically always produced with the $\bar{s}s$ pair having parallel spins [8]. How this comes about is uncertain. Possibly, this could be a fundamental feature of the $\bar{s}s$ production mechanism, or it could be related to a polarised $\bar{s}s$ -component inside the anti-proton/proton (polarisation meaning the direction, or orientation, of the spin). This intrinsic spin is however rather poorly known as it has been found that only a fraction of the spin is carried by the quarks [8].

The different models give different predictions for the correlation between the initial proton spin and the final state Λ spin and it is still unclear how the polarisation arises and s-quarks are created [8].

2.4.4 Hypernuclei

Hypernuclei are also of interest to PANDA. These are nuclei where (at least) one of the nucleons has been replaced by a hyperon. However, very different predictions for the spin-dependent contribution to the hyperon-nucleon interaction exist. A special γ -ray detector will be available at PANDA for investigating

excited hypernuclei by detecting the emitted photons from the de-excitation process with high resolution. With this technique, one will investigate the interactions between nucleons and hyperons. Also double hypernuclei and interactions between hyperons will be addressed [9].

Hyperatoms, where the atom contains a hyperon in an atomic orbit, are of interest for studies of hyperon properties. An especially interesting case is when the hyperon in the atomic orbit is a Ω^- -hyperon, because of its very long life time (82 ps) and its large spin of 3/2. A measurement of its electric quadrupole moment will give information on its shape, as well as the quark-quark interactions [9].

Chapter 3

FAIR and the PANDA Detector

3.1 The GSI and FAIR Facilities

Today the GSI facility includes a UNILNAC (heavy ion linear accelerator) delivering protons with an energy of up to 14 MeV/u, a heavy ion synchrotron (SIS) which accelerated particles to momenta of up to 2 GeV/u and an experimental storage ring (ESR) [10]. The future FAIR facility will be equipped with an additional double ring synchrotron (SIS100/300 for accelerations of heavy ion beams of up to 2.7 GeV/u and 34 GeV/u, respectively). The SIS100 ring will accelerate the protons which will be used to produce the secondary anti-proton beam. The ring has a circumference of 1100 meters and will be located 17 meters below ground. Three additional storage rings will be built: the CR (Collector Ring) where the anti-protons will be stochastically cooled, the NESR (New Experimental Storage Ring) and the HESR (High Energy Storage Ring). The HESR will store 10^{11} anti-protons with momenta between 1.5 and 15 GeV/c [9].

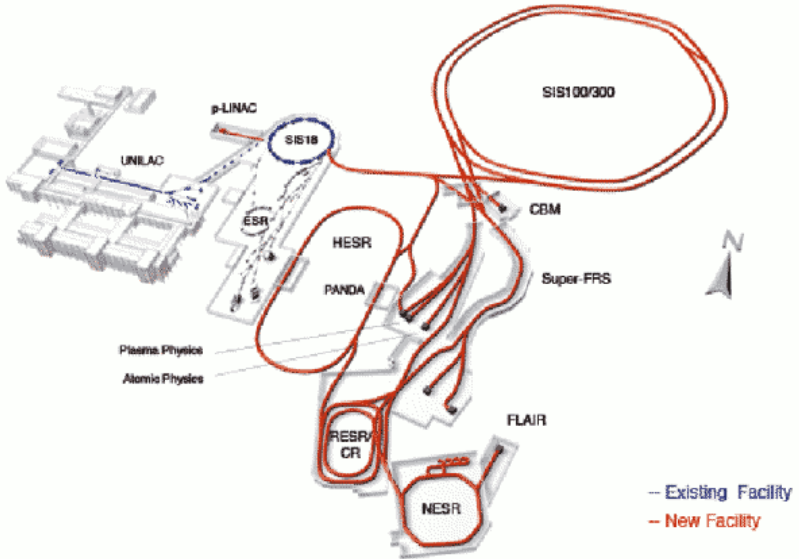


Figure 3.1: The figure shows the existing GSI and future FAIR facilities, marked with blue and red respectively [11].

High intensity beams of anti-protons will be used for atomic-, nuclear- and particle physics at FLAIR, CBM will study relativistic heavy ion reactions [12]. Radioactive nuclei beams having energies up to 1.5 GeV/nucleon will be available for Super FRS [3].

The cost of the new facility has been estimated to 1.2 billion Euros and it is planned to be completed in 2015 [11].

3.2 The PANDA Detector

The PANDA detector, which is foreseen to be commissioned in 2014 or 2015, is one of the largest experiments at the new facility. It is designed to provide a nearly full coverage of the solid angle with excellent energy and angular resolution for neutral and charged decay particles. The detector layout can be seen in Figure 3.2.

The detector consists of two spectrometers: a target spectrometer (TS) with a superconducting solenoid and a forward dipole spectrometer (FS) for particles with opening angles of more than $\pm 10^\circ$ in the horizontal and $\pm 5^\circ$ in the vertical plane. The maximum opening angles in the FS are approximately 22° in the vertical plane and slightly larger in the horizontal one.

More information on the topics in this chapter can be found in the PANDA Technical Design Report [13].

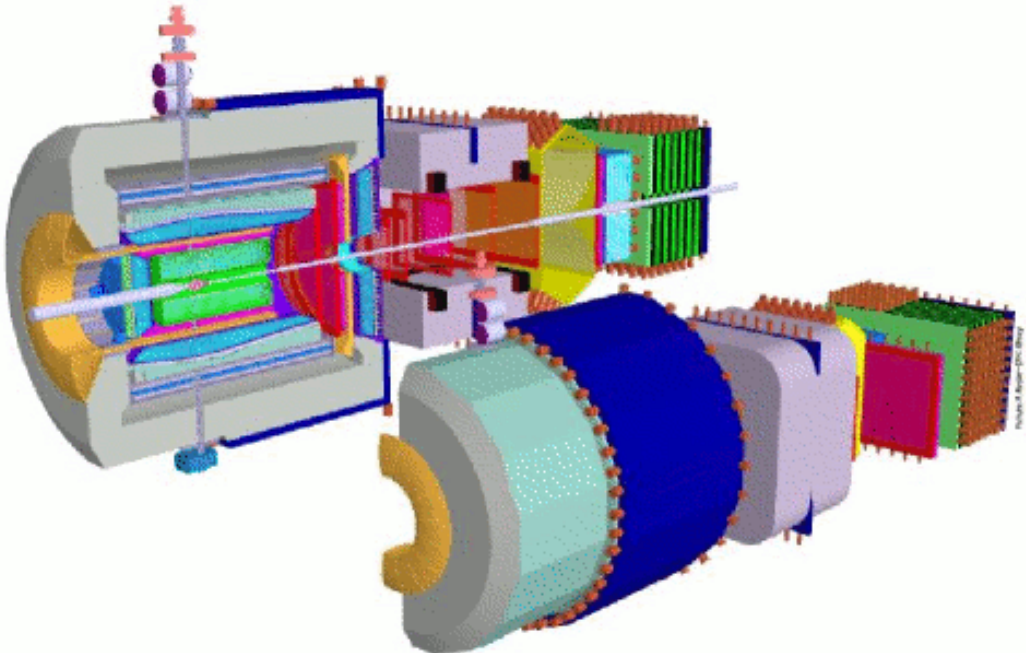


Figure 3.2: The design of the complete PANDA detector, as it was described in the Conceptual Design Report in 2001 [13].

3.2.1 The Target Spectrometer

The target spectrometer (TS) has a cylindrical geometry which surrounds the immediate interaction region and reaches out to a radius of about 2 meters. It can be seen in Figure 3.3 and includes the target system, a micro vertex detector (MVD), a straw tube tracker (STT) or alternatively a time projection chamber (TPC), a time-of-flight (TOF) detector, a detector for internally reflected Cherenkov light (DIRC) and an electromagnetic calorimeter (EMC). The coil of the solenoid magnet is placed outside of these sub-detectors. Muon detectors are placed outside the coil.

The Target

The target system for PANDA must deliver a target thickness that gives a luminosity of $2 \cdot 10^{32} \text{ /cm}^2\text{s}$. Assuming 10^{11} stored anti-protons in the HESR, this translates into a target thickness of about $4 \cdot 10^{15}$ hydrogen atoms per cm^2 . Two alternatives, a cluster jet target and a pellet target, have been proposed.

The cluster jet target is an internal gas system which uses a continuous stream of hydrogen cluster gas that is being directed at the interaction region. A continuous flow can be delivered but the desired target density has not been reached yet.

The pellet target is an approach which uses frozen droplets of hydrogen (pellets). Hydrogen gas is liquefied and cooled down before being injected into

a low pressure helium environment in form of a jet, which later breaks up to a uniform train of droplets. It is believed that this method can deliver the desired effective target thickness of $4 \cdot 10^{15}$ atoms/cm².

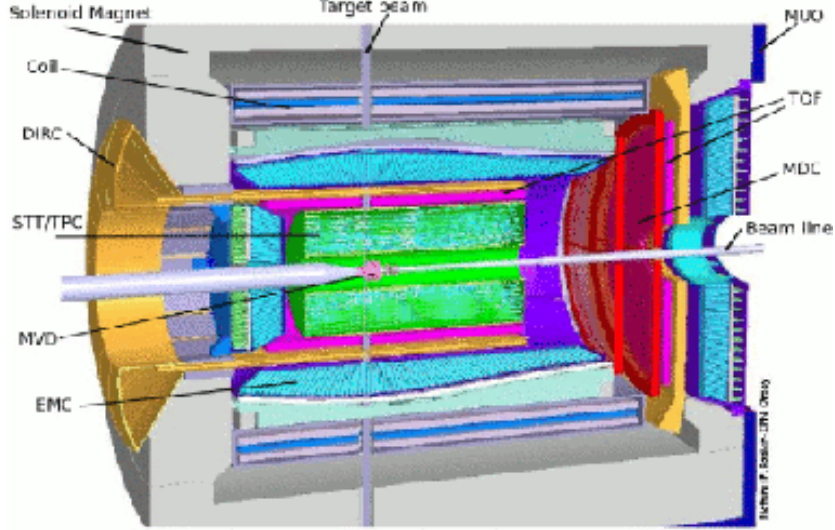


Figure 3.3: The layout of the target spectrometer with its sub-detectors [13].

The Micro Vertex Detector

The micro vertex detector (MVD) is a radiation hard silicon detector, especially designed to detect secondary vertices of, for example, the decays of strange and charmed hadrons. Therefore it is of utmost importance that it is located close to the interaction point.

The detector features a barrel section, most likely consisting of four layers and six forward discs. The two innermost barrel layers will be made with pixel geometry and the forward discs will contain a mix of pixels and strips [14]. The pixel size will most likely be $(100 \times 100) \mu\text{m}^2$ to ensure good resolution and radiation hardness close to the interaction point [14]. The two outermost barrel layers will consist of silicon strip detectors. The estimated spatial resolution of the detector is $100 \mu\text{m}$.

Tracking with the STT and the TPC

The outer tracking system consists of two parts, one which will be either of the straw tube tracker (STT) or the time projection chamber (TPC) type, and a second one consisting of Multi-wire Drift Chambers (MDCs) or Gas Electron Multipliers (GEMs).

The STT is a system of self-supporting gas filled straw detectors, arranged in 11 cylindrical and skewed double layers. The innermost layer has a radius of 16 cm and the outermost a radius of 42 cm. The total length of the detector will be 1.5 m. Charged particles entering the detector will produce electrons and positive ions that will drift in different directions in an electric field. Close

to the wire, which is on positive voltage, avalanche amplification will occur and the electrons will be collected here while the ions drift towards the cathode. The resolution perpendicular to the beam line is about $150\ \mu\text{m}$, depending on the drift distance [15]. The coordinates in the beam direction for this detector can be obtained in two ways. The first way is to use the charge division technique. The length-dependent wire resistivity affects the amplitude of the output signals and when reading out this at both straw ends, one can calculate where the interaction took place. The second way is to use the geometry of the skewed straws. The first technique is expected to give a resolution 0.5-1% of the sensitive wire length (which translates into 7-15 mm), a value which is approximately 2-3 times larger than the resolution from the second method. The drift time in the detector depends on the gas mixture filling the straws, but varies between tens of nano seconds up to a few hundred nano seconds [15].

The TPC is a much more complex detector than the STT and it is expected to give the best particle identification below momenta of $1\ \text{GeV}/c$. The detector itself is straight forward. However, the read-out electronics is very expensive and the online reconstruction is complicated. The TPC consists of two large gas filled cylindrical volumes with an electric field applied in the direction of the beam line. The field will separate electrons from positive gas ions created by traversing particles and the electrons will drift towards the readout anode end cap of the cylinder. Avalanche amplification will occur in Multi Wire Proportional Chambers (MWPCs), with the charge amplification most likely coming from GEMs. The read-out at the end cap will give two-dimensional information on the projection of the track. The third coordinate comes from drift time measurement of the primary electron clusters. The resolution for secondary vertices is foreseen to be $150\ \mu\text{m}$ in $r\varphi$ -direction and 1 mm along the beam axis.

After the STT/TPC there will be either two MDCs or two GEM detectors in order not to lose information on charged particles in the gap after the STT/TPC which would otherwise exist in the detector.

Charged Particle Identification

Charged particle identification in the target spectrometer is done using information from many sub-detectors. For instance, energy loss per path length in a medium is a useful method for particle identification when the signal amplitude, as well as space coordinates, are known. This is not a problem for the TPC-option, but for the STT it poses a challenge since not as many measurements per track are performed and therefore fluctuations in dE/dx can be large. Other identification techniques include time-of-flight measurements and Detection of Internally Reflected Cherenkov (DIRC) light.

The PANDA time-of-flight (TOF) stop counters will provide a stop signal with respect to the start signal (given most likely by the MVD close to the interaction point) as a particle traverses the target spectrometer. Given that the particle is not too fast in relation to the time resolution, one can obtain velocity information for the particle. The TOF will consist of two parts, a barrel shape outside the tracker and an end cap in the forward spectrometer. Both consist of plastic scintillators with channel-plate photo multiplier read-out that can operate in magnetic fields up to 2.2 T.

The DIRC identifies particles with momenta up to several GeV/c using totally internally reflecting Cherenkov photons and the best identification is done

for momenta above 1 GeV/c. As particles enter the quartz bar, some of the radiated Cherenkov photons will always be internally reflected. These photons can be focused onto an array of photo multipliers or avalanche photo diodes where the Cherenkov angle is measured from the radius of the Cherenkov ring. This ring can be used to determine the velocity of the particle. The velocity is then used for particle identification, together with the momentum information from the drift chamber.

The Electromagnetic Calorimeter

The electromagnetic calorimeter is by far the single most expensive sub-detector. It must be able to detect photons with both high and low energy, meaning that it must give position and timing resolution over a wide dynamic range from tens of MeV up to several GeV. The proposed material for this is lead tungsten, PbWO_4 , a radiation hard and compact crystal which is a recently developed scintillator that has been chosen for other high-energy physics experiments such as CMS and ALICE at CERN.

The barrel part of the calorimeter will be 2.5 m long and filled with 11360 tapered crystals of 18 different shapes making sure there is a tilt towards the interaction point and as small gaps as possible between the individual crystals. The length of the crystals in the barrel part is expected to be 20 cm (≈ 22 radiation lengths), while the 3864 crystals in the forward end cap may be longer [16]. The backward end cap will contain 816 crystals.

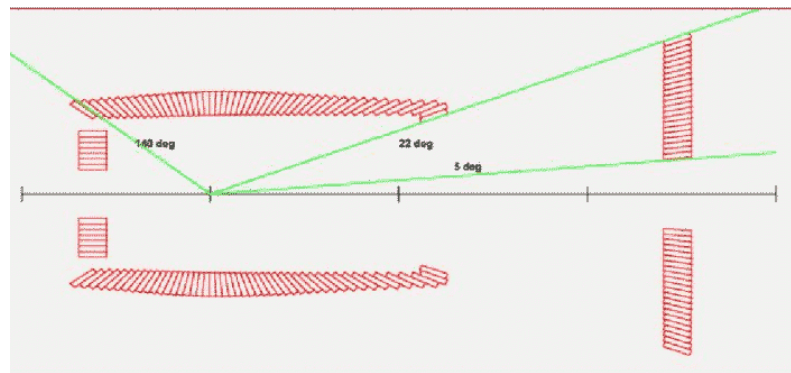


Figure 3.4: The electromagnetic calorimeter in the target spectrometer with the barrel part, as well as the forward and backward end caps [13].

Because the calorimeter will be located in the solenoid, the read-out has to be made using light sensors that are insensitive to magnetic fields. This excludes the choice of photo multiplier tubes and most likely the read-out will be made using Avalanche Photo Diodes (APDs) in the barrel and the end-cap. Vacuum triodes are considered for the forward end-cap due to the high count rate in this region.

As the light yield of PbWO_4 is relatively low compared to many other scintillators used in calorimeters, much effort goes into increasing the light yield. One way to do this is to cool the detector, as will be discussed in section 4.3.

The Magnet System

Outside of the calorimeter there will be a superconducting coil with an inner radius of 90 cm and a length of 2.8 m, generating a field strength of 2 T.

Muon Detectors

Muon detection will be done using one of three alternatives. The first is to use scintillator counters for time-of-flight measurements, the second is to use electromagnetic and hadronic calorimetry to measure dE/dx and the third to use muon tracking. The muon tracking can be done either using Mini-Drift Tubes based on the Iarocci principle but operated in proportional mode, or drift tubes similar to those used for CMS at CERN. Also a combination of both types of mini-drift tubes is possible.

3.2.2 The Forward Spectrometer

The forward spectrometer consists of a large, normally conducting dipole magnet, six Multi-wire Drift Chambers (MDCs), possibly a Ring imaging Cherenkov Detector (RICH), a second electromagnetic calorimeter (F-EMC), a hadronic calorimeter (H-EMC) and a muon detector.

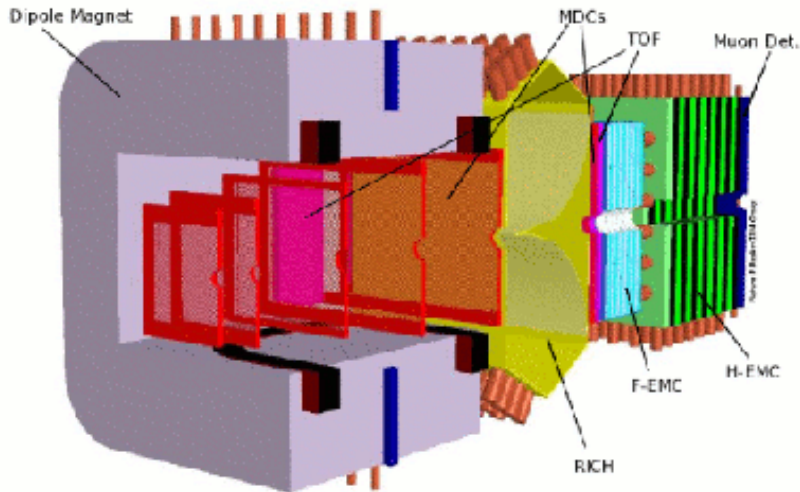


Figure 3.5: The forward spectrometer with named sub-detectors [13].

The Magnet System

The dipole magnet in the forward spectrometer will bend the charged particles to allow for a momentum analysis. The maximum bending power is 2 Tm, causing a bending of 2° for the most energetic particles. The anti-proton beam will be deflected and bent back using a chicane to prevent interference.

Tracking

Particles emitted at angles lower than 22° will not be fully covered by the central tracking and therefore it was initially suggested to put additional MDCs located 1.4 and 2 m downstream of the target, inside the magnet. Another pair of planar MDCs were discussed to be placed after the magnet to measure the deflections in the forward spectrometer dipole magnet, as well as a third pair located in the dipole magnet gap to trace low momentum particles.

The drift chambers are planned to be 1 cm thick and contain squared drift cells made up from cathode and sense wires mounted on self-supporting frames. The first two MDCs contain four pairs of octagonal detection planes in different angles, while the others are grouped in three double layers.

Particle Identification

The time-of-flight (TOF) wall will be located approximately 7 m from the interaction point. It is equipped with strips of plastic scintillators with photo multiplier read-out. The expected time resolution is 50 ps, which will be enough to distinguish pions from kaons at 2.8 GeV/c and pions from protons up to 4.7 GeV/c. A Ring Imaging Cherenkov Detector (RICH) will be probably be required for particle identification at higher momenta.

The Forward Electromagnetic Calorimeter

The forward electromagnetic calorimeter is planned to be a Shashlyk-type detector with alternating layers of lead and plastic scintillators for detecting photons and electrons. The scintillators are used for detection, while the lead layers act as energy absorbers and photon converters. The read-out will be done using wavelength shifting fibres and photo multipliers.

The Hadronic Calorimeter

The second part of the forward calorimeter is the multi-purpose hadronic calorimeter. Firstly, it is designed to measure neutral hadrons like neutrons and anti-neutrons which are not detected anywhere else. Secondly, it will serve as a fast trigger for reactions with forward scattered hadrons. Thirdly, it will act as a muon filter for the muon detectors placed at the very end.

The calorimeter which will be used for this already exists. It comes from the WA80 experiment at CERN and has an electromagnetic and a hadronic section. The scintillator used in this detector is called PS-15A and it is based on polymethylmethacrylate (PMMA).

The Muon Detectors

The final design for this detector part is not finished but it is under discussion to use the same principle as for the target spectrometer muon tracking.

Chapter 4

Energy Measurements with Crystals

4.1 Particle Interactions in Scintillators

4.1.1 Photon Interactions with Matter

There are three principal ways photons can interact with matter: via the *photoelectric effect*, *Compton scattering* and *pair production*. The probability for the processes are strongly dependent on the energy and the atomic number of the material (Z), as can be seen in Figure 4.1.

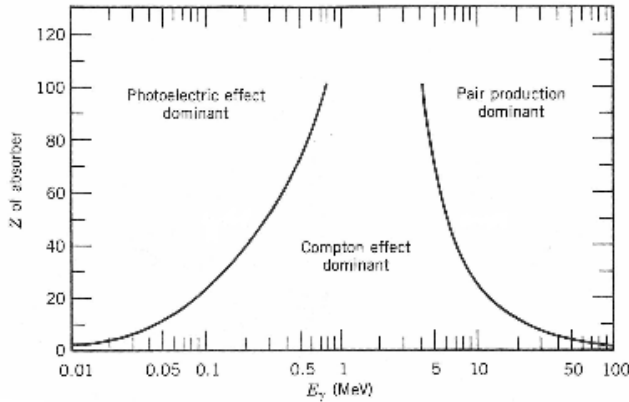


Figure 4.1: Different photon interactions with matter and their dominating regions [17].

Photoelectric absorption dominates for low energies, where the incoming photon ejects an electron from the material, resulting in a released electron with an energy equal to the energy of the photon minus its binding energy with which the electron was bound [17]. Experimental results have indicated a cross-section [18]

$$\sigma_{\text{ph}} \propto \frac{Z^5}{E_\gamma^{7/2}} \quad (4.1)$$

in the low energy regime and [18]

$$\sigma_{\text{ph}} \propto \frac{Z^5}{E_\gamma} \quad (4.2)$$

for $E_\gamma \gg m_e c^2$, where Z is the atomic number of the material and E_γ the photon energy.

Compton scattering is a process in which the incoming photon scatters from a loosely bound atomic electron, which can be considered to be at rest. The result is a scattered photon and a scattered electron sharing the available energy. The cross-section for this process reduces to the Thomson scattering cross section at low energies.

$$\sigma d\Omega = \frac{e^2}{4\pi m c^2} (\epsilon_i \cdot \epsilon_f)^2 d\Omega \quad (4.3)$$

with ϵ being the polarisation of the initial and final photon [19]. This is a non-relativistic description of scattering of electromagnetic radiation. At energies where $E_\gamma \gg m_e c^2$, the cross-section for Compton scattering is proportional to [18]

$$\sigma_{\text{Co}} \propto \frac{Z \ln E_\gamma}{E_\gamma}. \quad (4.4)$$

Pair production is a process occurring in the neighbourhood of a nucleus (to conserve momentum), in which the photon converts into a electron-positron pair in the presence of an electromagnetic field. The threshold energy is twice the electron mass and the cross-section of the process can be approximated as

$$\sigma_{\text{pair}} \propto Z^2 \ln 2E_\gamma. \quad (4.5)$$

Pair production is related to *bremsstrahlung* where electromagnetic radiation is emitted as a result of an electrically charged particles being scattered in an electric field [20]. Since bremsstrahlung depends on the strength of the electric field, screening of the nucleus from the surrounding electrons is an important factor. Also for pair production this will be the case. The cross-section for pair production thus depends on the screening effect parameter ξ given by [20]

$$\xi = \frac{100 m_e c^2 E_\gamma}{E_{e^+} E_{e^-} Z^{1/3}}. \quad (4.6)$$

When $\xi=0$, there is complete screening and for $\xi=1$ there is no screening. For photon energies

$$E_\gamma \gg \frac{m_e c^2}{\alpha Z^{1/3}} \quad (4.7)$$

$\xi \rightarrow 0$, giving complete screening [20]. Here, α is the electromagnetic coupling constant. When there is no screening, one can calculate an energy-independent expression for the pair production cross-section [20]

$$\frac{1}{\lambda_{\text{pair}}} = N\sigma_{\text{pair}} \approx \frac{7r_e^2}{9} \quad (4.8)$$

with N being the density of atoms. It is related to the radiation length X_0 (see section 4.1.2) through [20]

$$\lambda_{\text{pair}} = \frac{9}{7}X_0. \quad (4.9)$$

An electromagnetic cascade with continuous pair production spreads in both transversal and longitudinal direction. A measure of the former is given by the so-called *Molière radius* of the scintillator.

4.1.2 Electron Interactions with Matter

Electrons scatter via Coulomb interactions in the material and due to their low mass, they will be largely deflected. Depending on how they are scattered, they will travel different distances, or ranges, in the material. In addition, due to the scattering they will change the direction and magnitude of their velocity and therefore be subjected to accelerations and emit bremsstrahlung [17].

The expressions for the energy losses per unit path length that the electron suffers is given by the Bethe-Bloch equation [17], which has contributions from both collisional and radiative losses

$$\frac{dE}{dx} = \left(\frac{dE}{dx} \right)_{\text{coll}} + \left(\frac{dE}{dx} \right)_{\text{rad}}, \quad (4.10)$$

$$\begin{aligned} \left(\frac{dE}{dx} \right)_{\text{coll}} &= \left(\frac{e^2}{4\pi\epsilon_0} \right)^2 \frac{2\pi N_0 Z \rho}{mc^2 \beta^2 A} \\ &\times \left(\ln \frac{T(T+mc^2)^2 \beta^2}{2I^2 mc^2} + (1-\beta^2) - (2\sqrt{1-\beta^2} - 1 + \beta^2) \ln 2 + \frac{1}{8}(1-\sqrt{1-\beta^2})^2 \right) \end{aligned} \quad (4.11)$$

$$\left(\frac{dE}{dx} \right)_{\text{rad}} = \left(\frac{e^2}{4\pi\epsilon_0} \right)^2 \frac{Z^2 N_0 (T+mc^2) \rho}{137 m^2 c^4 A} \left(4 \ln \frac{2(T+mc^2)}{mc^2} - \frac{4}{3} \right) \quad (4.12)$$

with T being the kinetic energy of the electron, N_0 Avogadro's constant, Z the atomic number, A the atomic weight and ρ the density of the material which the electron traverses. The electron mass is denoted m .

The radiative term plays a larger role for high energies and heavy materials.

Radiation Length

Radiation length is a concept frequently used in describing the characteristics of a detector material. It corresponds to the distance the electron has travelled when its energy has been reduced by a factor $1/e$, due to radiation losses only. For the high energy limit where collisional losses can be ignored to radiative ones, the radiation length becomes basically independent of the energy and is given by [20]

$$\frac{1}{X_0} \approx \frac{4r_e^2 \alpha \rho N_A Z (Z+1)}{A} \ln \left(\frac{183}{Z^{1/3}} \right) \quad (4.13)$$

where r_e is the classical radius of the electron, N_A Avogadro's constant and A the atomic number.

4.2 Energy Resolution

When measuring a quantity (the incoming γ energy in this case) there are always errors associated with the measurement, which makes the measured value fluctuate around an average value. In this particular case contributions come from statistical fluctuations, due to the Poisson statistics of the collected light in a scintillator, fluctuations associated with electronic noise and other instrumental effects. The relative influence of these different effects are generally not known in detail, but can be estimated from the energy dependence of the measured total fluctuation of the signal (the RMS-width σ or the Full Width at Half Maximum, FWHM, of the peak in a measurement where the incoming photon energy is known). If we assume that the measured quantity x depends on many parameters $u, v, \dots, x=f(u, v, \dots)$, then the variance of x can be expressed as [21]

$$\sigma_x^2 = \lim_{N \rightarrow \infty} \frac{1}{N} \sum \left((u_i - \bar{u}) \left(\frac{\partial x}{\partial u} \right) + (v_i - \bar{v}) \left(\frac{\partial x}{\partial v} \right) \right)^2. \quad (4.14)$$

For uncorrelated quantities, the above relation reduces to

$$\sigma_x^2 = \lim_{N \rightarrow \infty} \frac{1}{N} \sum \left((u_i - \bar{u})^2 \left(\frac{\partial x}{\partial u} \right)^2 + (v_i - \bar{v})^2 \left(\frac{\partial x}{\partial v} \right)^2 \right) = \sigma_u^2 \left(\frac{\partial x}{\partial u} \right)^2 + \sigma_v^2 \left(\frac{\partial x}{\partial v} \right)^2. \quad (4.15)$$

Thus we see that the variance can be written as a sum of individual contributions $\sigma_{x,u} = |\sigma_u \cdot dx/du|$, $\sigma_{x,v} = |\sigma_v \cdot dx/dv| \dots$. For detecting photons from a scintillating crystal, one contribution is due to the Poisson statistics of the light collection process. Since the variance in the number of photo electrons at the cathode equals that number, the contribution $\sigma_{E, Poisson}$ to the uncertainty of the measured energy is proportional to the square root of the energy:

$$\sigma_{E, Poisson} = a \cdot \sqrt{E} \quad (4.16)$$

For scintillators having a high light yield this term is expected to only give a small contribution to the relative energy resolution, since the number of photons produced per incoming MeV is relatively large. For PbWO_4 (see section 4.3) this is not the case, it is therefore very important to ensure a high efficiency in collecting the photons which are created. This can be done using a good reflective wrapping material and a good optical coupling between the PM tube and the crystal [18].

The electronic noise describes the errors arising from the electrical set-up used for the measurements. The noise depends on the actual setting of the electronics such as high voltage etc, but does not depend on the signal strength and is thus independent of the energy:

$$\sigma_{E, \text{Noise}} = b \quad (4.17)$$

Lastly, one could in addition expect some fluctuations in the measured signal due to crystal properties such as non-uniformity of the produced light inside the crystals, temperature gradients, detector ageing, radiation damage etc. For a system of crystals errors in the inter-calibration will contribute. These fluctuations will be proportional to the signal strength, thus proportional to the energy:

$$\sigma_{E, \text{Crystal}} = c \cdot E \quad (4.18)$$

This term often dominates the energy resolution because the two other terms tend to be small [18]. Only for detectors where special care has been taken to prevent shower leakage and to inter-calibration errors, this term can be manageable [22].

The energy resolution of scintillating crystals is thus often written as:

$$\sigma^2 = \sigma_{E, \text{Poisson}}^2 + \sigma_{E, \text{Noise}}^2 + \sigma_{E, \text{Crystal}}^2 = a^2 E + b^2 + c^2 E^2 \quad (4.19)$$

This can also be written as [1]

$$\frac{\sigma}{E} = \frac{a}{\sqrt{E}} \oplus \frac{b}{E} \oplus c, \quad (4.20)$$

where the \oplus sign indicates quadratic summing.

4.2.1 Energy Resolution for PANDA

The electromagnetic calorimeter plays a decisive role for most of the physics programs of PANDA and it must be able to cover a very large dynamic range (from tens of MeV to several GeV) of photons. Low energy thresholds are required for proper scans of mass and widths of channels with photons coming from isolated decays (photons from other decays but π^0) such as $\bar{p}p \rightarrow \eta_c \rightarrow \gamma\gamma$ and $\bar{p}p \rightarrow h_c \rightarrow \eta_c \gamma \rightarrow \gamma\gamma\gamma$. The problematic backgrounds come from the high cross-section channels such as $\bar{p}p \rightarrow \pi^0 \gamma \rightarrow \gamma\gamma\gamma$ and $\bar{p}p \rightarrow \pi^0 \pi^0 \rightarrow \gamma\gamma\gamma\gamma$, where one photon is not detected [23]. These channels pose big challenges as the signatures look the same as for the true signal. For example, upper limits for the signal-to-background ratio for $\bar{p}p \rightarrow \eta_c \rightarrow \gamma\gamma$ have been estimated for different energy thresholds, assuming 100% detector efficiency[24]. For a threshold of 15 MeV the ratio was 1.75, for 10 MeV it was 2.82 and for 5 MeV it was 7.6. Corresponding Geant4 simulations have given signal-to-background ratios of 1.1 for 25 MeV and 0.7 for 50 MeV. The results were based on an energy resolution where $\sigma_{E, \text{noise}} = 1.3$ MeV. 50 photo electrons were assumed to be emitted per MeV at -25 °C. [9].

Other problems come from the low mass of the pions and the forward boost of the system. This can cause very low energy photons to be emitted (for instance, a 1 GeV/c pion can emit a 4 MeV photon [23]) and if such a photon is lost it is not possible to distinguish the signal from the background. The dependence of the photon energy on the momentum of the pion is shown in Figure 4.2.

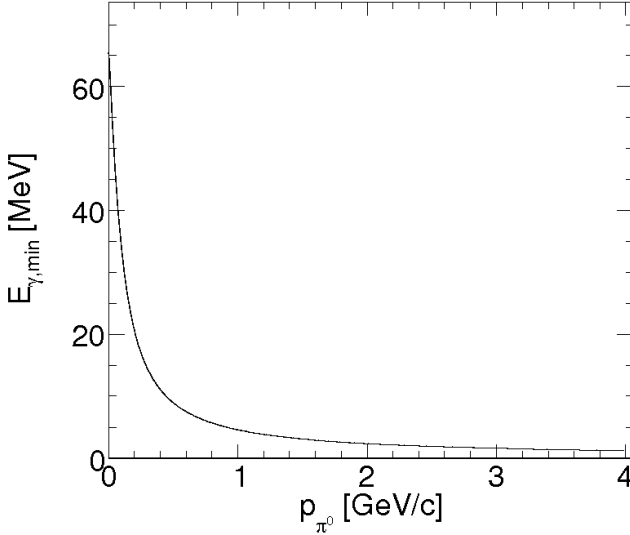


Figure 4.2: The minimum energy of a decay photon as a function of the pion momentum [23].

A third reason for the importance of a good calorimeter is to distinguish radiative (charmonium) decays from (for instance) charmed hybrids or glueballs that involve pions or etas ($\bar{p}p \rightarrow \chi_{c1,2,3} \rightarrow J/\psi\gamma$ with a background of $\bar{p}p \rightarrow J/\psi\pi^0$). Either the π^0 is needed to reconstruct the particle itself, or to reject the background. This is why the PANDA collaboration envisages a detector which can measure photon energies down to approximately 10 MeV. A high efficiency in detecting particles is crucial and a good energy resolution desired.

Excellent energy resolution is needed in the range of 100 MeV-1 GeV where many important channels decay to π^0 , and η , which then decay into photons (such as for instance $\psi \rightarrow J/\psi \rightarrow \pi^0\pi^0$, $X \rightarrow \chi_{c1} \rightarrow \pi^0\pi^0$, $X \rightarrow \eta_c\pi^0\pi^0$). The mass of a particle decaying to two photons is measured by the invariant mass M^2 ,

$$M^2 = (E_1 + E_2)^2 - (\mathbf{p}_1 + \mathbf{p}_2)^2 = \frac{1}{c^2} \sqrt{2E_1 E_2 (1 - \cos \alpha)} \quad (4.21)$$

where E_1 and E_2 are the energies of the decay particles, p_1 and p_2 the momentum vectors and α the angle between them. The mass resolution is dominated by the resolution of the lowest energy photon

$$\begin{aligned} \sigma_{m_{\gamma\gamma}} &= \sqrt{\left(\frac{\partial m_{\gamma\gamma}}{\partial E_1} \sigma_{E_1}\right)^2 + \left(\frac{\partial m_{\gamma\gamma}}{\partial E_2} \sigma_{E_2}\right)^2 + \left(\frac{\partial m_{\gamma\gamma}}{\partial \alpha} \sigma_\alpha\right)^2} \\ &= \frac{m_{\gamma\gamma}}{2} \sqrt{\left(\frac{\sigma_{E_1}}{E_1}\right)^2 + \left(\frac{\sigma_{E_2}}{E_2}\right)^2 + \left(\frac{\sin \alpha}{1 - \cos \alpha} \sigma_\alpha\right)^2} \quad (4.22) \end{aligned}$$

It is therefore important to ensure a good detection of the low energy photon so that the decay particle can be identified.

The granularity (position resolution) is given by geometrical constraints of the sub-detectors as well as the scintillator material, and it is important to have a good enough position resolution to reconstruct the opening angles of the π^0 . This is mainly a problem for high π^0 -momenta since it implies small opening angles. This effect is most important for the forward directions.

4.3 PbWO₄ Scintillator Characteristics

Lead tungsten crystals, PbWO₄ or PWO, were developed for the new generation of high-energy physics experiments at LHC, CERN. Today it is being used in the electromagnetic calorimeter of CMS, in PHOS and in the photon spectrometer of ALICE. A photograph of a typical crystal can be seen in Figure 4.3.

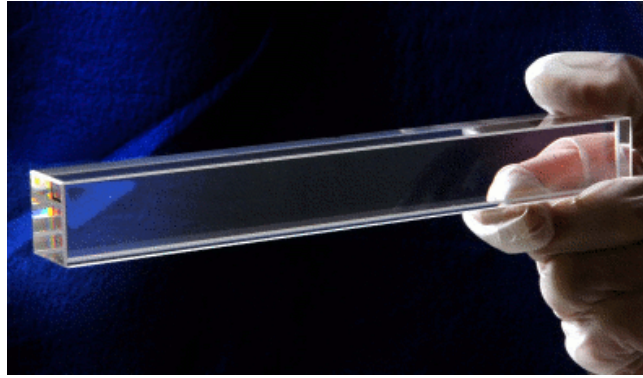


Figure 4.3: One of the PWO crystals which has been delivered to Uppsala for future measurements of energy resolution and light yield uniformity. Photograph by [25].

The crystal development processes for these experiments have yielded high-quality and radiation hard crystals. More specifically, it seems the doping of the crystals is the key to limiting the reduction of the optical transmission to tolerable levels [4]. Adding of trivalent rare earth ions (having atomic numbers between 58 and 70) to the crystal lattice makes inner shell transitions possible [26] and decreases cation and anion (i.e. positively and negatively charged ion) vacancies in the crystal. Unfortunately, addition of these ions also creates shallow electron centres which quench the scintillator light [4]. Some properties of lead tungstate are displayed in Table 4.1.

The very high density and short radiation length of PWO allows for a very compact detector. The high index of refraction is a very good quality since it reduces the risk of light scattering out of the crystal. The fast decay time allows for a high count rate.

The doping of PWO is essential to increase the low light yield, and so far PANDA has investigated crystals doped with impurities of Mo, La, Tb and Y [27]. The light yield from PWO crystals has been measured to approximately 25 phe/MeV at room temperature [28]. However, the light yield from PWO is very temperature dependent and increases with about 2% per lowered degree C

Property	PWO
Density [g/cm ³]	8.28 [27]
Radiation length [cm]	0.89 [27]
Molière radius [cm]	2.2 [22]
Refractive index	2.3 [27]
Decay time [ns]	5/15/100 [22]
Light Yield at 18 °C [phe/MeV]	20 [27]

Table 4.1: Some properties of lead tungsten. “phe” is short for “photo electrons” and the three decay times correspond to the fast, medium and slow components.

at 10 °C, see Figure 4.4.

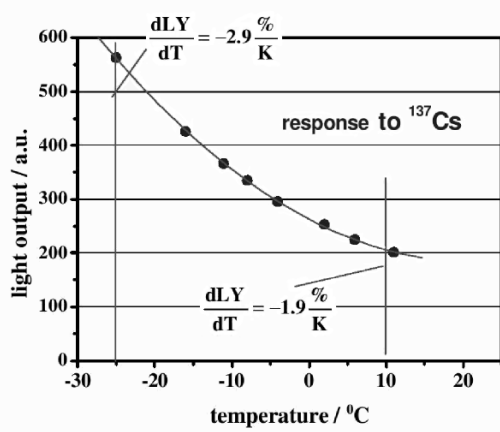


Figure 4.4: The light yield of PWO as a function of the temperature [29].

Chapter 5

Energy Resolution Measurements with PANDA Crystals

5.1 The Tagged Photon Facility at MAX-Lab in Lund

The electron accelerator facility MAX-Lab in Lund has been used to investigate the response of PWO crystals at low energies. The facility consists of three rings called MAX I, MAX II and MAX III that are used for research with synchrotron radiation (electromagnetic radiation emitted when ultra-relativistic charged particles move through a magnetic field). An overview of MAX-Lab can be seen in Figure 5.1.

The first step of the accelerator system is the pre-accelerator system. It consists of an electron gun, a linear accelerator and a recirculation system. After passing these three stages the electrons have reached an energy of 250-500 MeV. At this point they are injected into the storage rings where they are further accelerated. The energy of the electrons in the MAX I storage ring is approximately 550 MeV, about 1.5 GeV in the MAX II ring and 700 MeV in the MAX III ring [30].

For nuclear physics applications, the electrons from MAX I are extracted and transferred to the tagging spectrometer region. Here they will impinge on a radiator and photons will be emitted due to bremsstrahlung. The post-bremsstrahlung electrons are detected with a spectrometer [31].

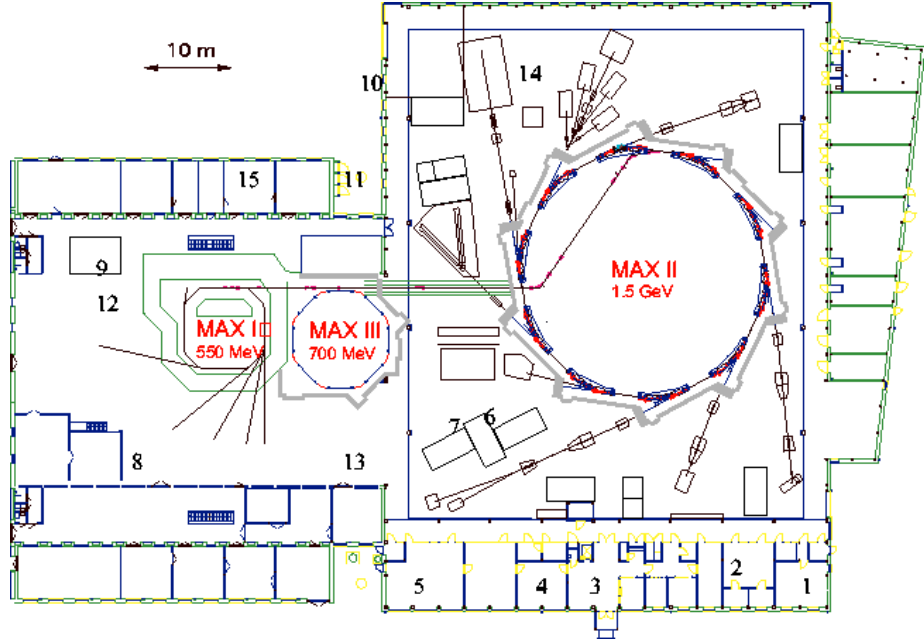


Figure 5.1: Overview of the MAX-Lab facility [32].

There are two tagging spectrometers, the first of which is a so-called end-point tagger capable of tagging photons close to the bremsstrahlung end point. The second tagger is the main tagger which can handle larger momentum values [33].

The tagging system consists of two rows of overlapping plastic scintillators, 31 in the first row and 32 in the back row. All scintillators are 25 mm wide and they overlap to 50% of their width in the plane perpendicularly to the electron paths, see Figure 5.2. The tagger signal is generated when a coincidence between two overlapping scintillators is registered. In total there are 62 tagged focal plane channels [33].

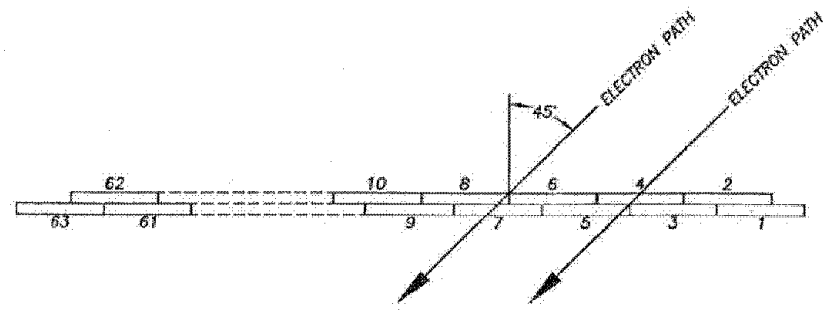


Figure 5.2: The scintillator arrangement for the tagging system at MAX-Lab in Lund [33].

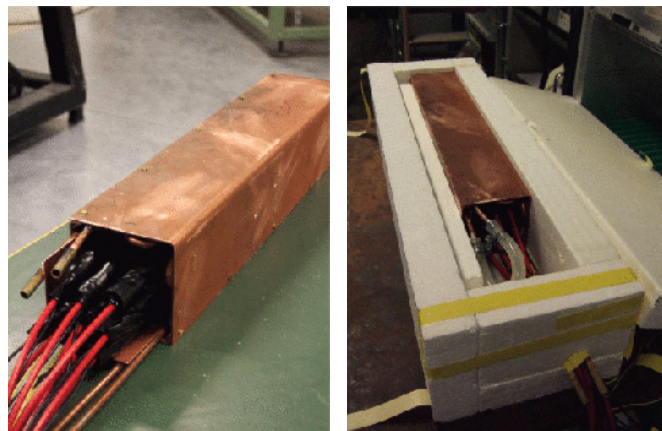
5.2 Measurement Set-up

Two different sets of runs have been performed at MAX-Lab, one taking place in April 2007 and the other in September 2007. The purpose of the measurements was to investigate the energy resolution of PWO crystals between 19 and 55 MeV. Both measurements involved cooling, but the equipment used was more advanced for the September measurement. In addition to better and more stable cooling, the time information from the crystal read-out was saved during this run measurement and was later used during the analysis for background rejection.

The crystal set-up used for both experiments was a 3×3 -array of PWO crystals from Bogoroditsk in Russia, each with the dimension $2 \times 2 \times 20$ cm 3 . Also a tenth PWO crystal was used and put on top of the set-up, perpendicular to the other nine crystals, to act as a detector for cosmic muons.

The signals were read out using Philips XP1911 Photo Multiplier Tubes (PM tubes). The polished crystal surfaces were wrapped with the mirror-like reflective foil VM2000 provided by 3M [34]. The crystals were attached to the PM tubes with VISCASIL silicon fluid (by General Electric) as an optical coupling, before being covered with black shrinking tape to prevent light leakage and to increase the stability.

For cooling, two different set-ups were used. For the April measurement, a small cooling machine with circulating cooling liquid was connected to a copper box surrounding the crystals. The copper block was then put inside an insulating box and kept with an over-pressure of nitrogen to prevent air from leaking in. The set-up is shown in Figure 5.3. The temperature at which the measurement was performed was -15 °C. Thermo elements were used to measure the temperature. The monitoring of the temperature was done with a web camera which was directed at the display of the thermo elements read-out.

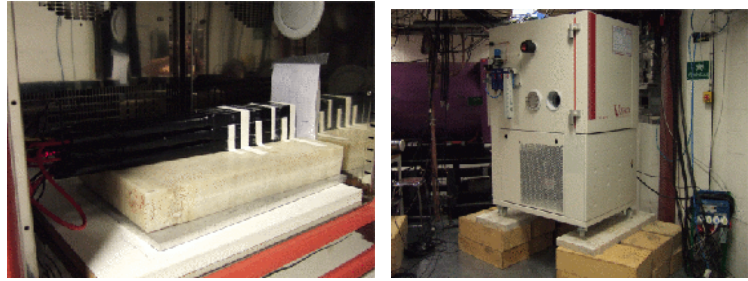


(a) The copper shell with the cooling pipes.
(b) The set-up in the isolating box.

Figure 5.3: The crystal set-up used for the first measurements.

For the September measurement, a climate chamber (Vötsch 4021) was available, in which it was possible to put the whole crystal array. It was cooled to

-25 °C, with an uncertainty of 0.1 °C. The climate chamber included a machine which dehumidified the air to ensure no ice would form on the cabling inside the chamber. The temperature inside the crystal array was not measured during the run, but from earlier investigations it was known that temperature inside the array stabilised around the set value after approximately 2h.



(a) The crystal array inside the chamber. (b) The climate chamber in place at MAX-Lab.

Figure 5.4: The crystal set-up for the September measurements with the crystal array and the climate chamber

The position of the beam spot was mapped using a laser to make sure the photons would go into the center crystal. For the second measurement, the beam was let in through a hole in the side of the chamber which was covered with a rubber lid. The probability for photon interaction in this material is very low and most photons will pass right through it. Those few photons that do interact are most likely scattered out of the direction of the beam and will not cause any problems.

5.3 The Read-Out Electronics

The electronical set-up used in both measurements were basically identical and can be seen in Figure 5.5.

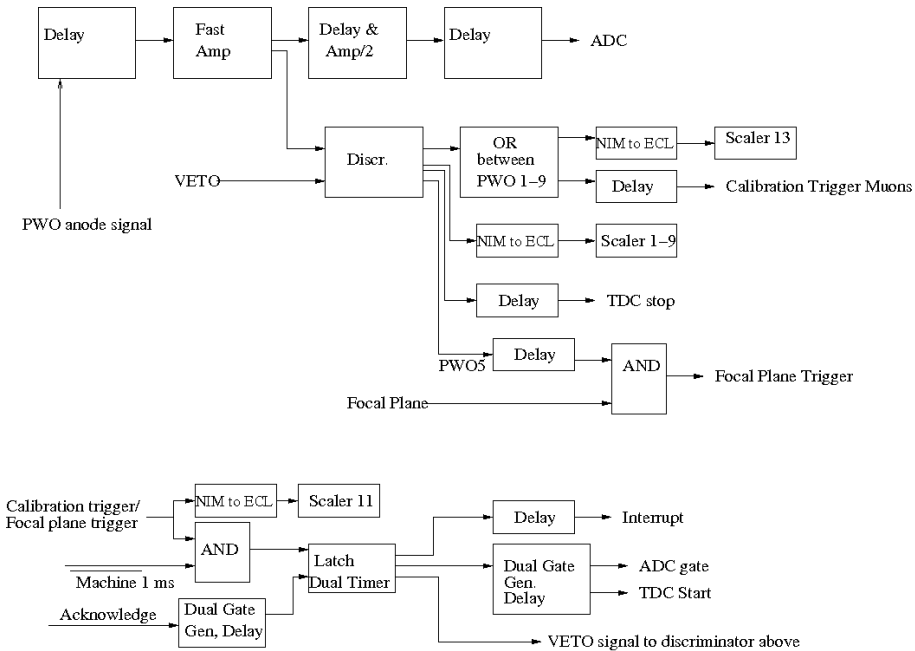


Figure 5.5: The electronic set-up used for the September experiments.

The signals from the nine crystals in the array were amplified and delayed in order to meet the timing requirements. Two different triggers could be used, one for triggering on cosmic muons for calibration purposes and one for triggering on the signal from the tagger focal plane in coincidence with the central crystal. The trigger took the data acquisition system into account by making sure that data was recorded when a detector had triggered and that no new events were processed while the system was busy. The Machine corresponds to a signal from the accelerator, inhibiting any trigger generation during the first 1 ms of the machine cycle. The “Acknowledge” is a signal sent from the data acquisition system to mark that the information has been saved and the system is ready to treat new signals.

The only difference between the electronical set-ups used for the two measurements is that the timing information from the PWO signals was not recorded for the April measurement, but for the September measurement it was. In April, the timing was adjusted so that the true coincidences were recorded, but there was no TDC-information and therefore it was not possible to reduce the number of random coincidences by narrowing down the time interval.

5.4 Analysis

As soon as the photons reach the center crystal of the array, the shower process begins in both lateral and transversal directions, resulting in energy deposits in the central as well as in the surrounding crystals. The raw spectra for the September measurements can be seen in Figure 5.6. The spike in the central detector around channel number 1900 is an overflow peak, which collects signals with higher energies than the maximum value and puts them in a certain (or a few) bin(s).

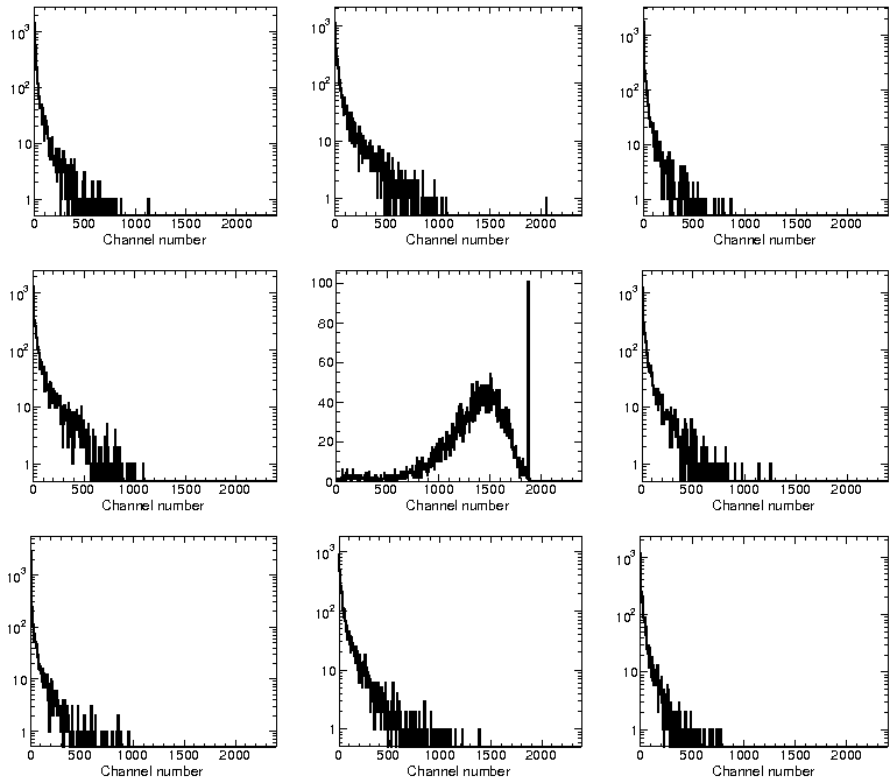


Figure 5.6: A typical energy deposits in the nine PWO crystals from the September measurements.

To obtain the energy resolution of the matrix, these energy contributions must be summed event wise. This is done using the CERN analysis program ROOT [35], but first all nine detectors must undergo a relative calibration using the zero point energy as well as another energy point. A threshold level for the addition of contributions was set to prevent noise from being added.

The timing information from the 62 focal planes detectors, and in the case of the September measurement also the center PWO timing information, were used to add the energy contributions for each event. The resulting peak which was obtained was then fitted with a Gaussian distribution and the mean position as well as the sigma were used to determine the energy resolution.

5.5 Relative Calibration

For the April measurement, a pedestal run was performed where the trigger signal came from the tenth crystal, located on top of the crystal array. The zero point energy could be extracted by fitting a Gaussian distribution to the noise peak. The second energy point was taken from the muon spectrum which was recorded during an over-night run. The threshold levels used in the analysis were chosen such that they were just above the energy at which the pedestal peak ended. The numerical values were between 0.3 and 0.9 MeV for the nine crystals, the large values stemming from some very wide pedestals.

Correspondingly, for the September measurement the two calibration points were taken from the zero point energy and a muon spectrum. The zero point energy was obtained from a pedestal run and the peaks were fitted with Gaussian distributions to obtain a mean value. The thresholds were determined in the same way as for the April measurements. The intervals for the thresholds were between 0.2 and 0.5 MeV. The second energy used for the calibration came from detected cosmic muons and the spectra can be seen in Figure 5.7. To get the position of the peak, Gaussian distributions were fitted around the muon peak.

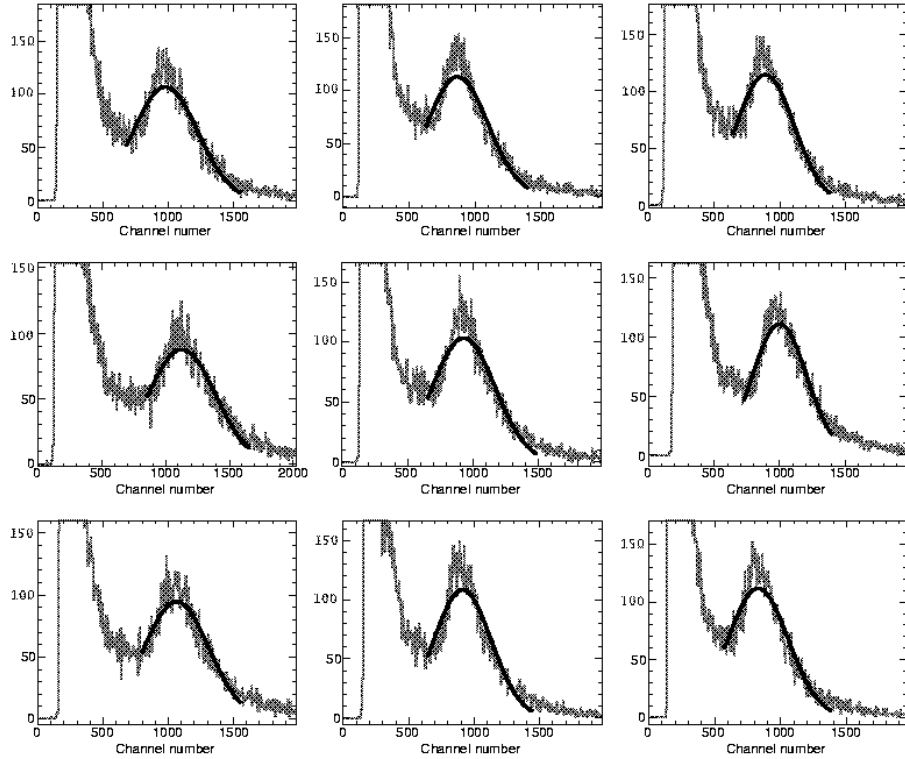


Figure 5.7: The recorded muon spectrum from the September measurements.

The widths (σ) of the muon peaks vary between 6.5 and 7.6 MeV for the nine crystals, the center crystal having a muon peak with $\sigma=6.9$ MeV. Depending on the interval chosen around the peak, the peak position changes by some hundred keV (<0.5 MeV).

Generally speaking, one may encounter some calibrational problems when using cosmic muons for calibration and a tagged low energy photon beam for measurement. The problem arises because the energy deposits inside the crystals from the muons and the photon beam take place at different locations. The cosmic muons will hit the crystal from above, along the whole length. The photons are directed to the front end side of the crystal array and will deposit their energy in that part. If the light yield along the crystal is uniform, this is not a problem. However, in chapter 6 where light yield uniformity is investigated, one clearly sees a dependence of the light yield on the distance between the incoming photon and the PM tube. If, however, the light non-uniformity is identical for all detectors, the relative calibration is not affected.

For one of the non-tapered crystals (crystal label 20_216) wrapped in VM2000, the average number of emitted photo electrons per incoming MeV (phe/MeV) over the whole crystal length is 40.1. If one only considers the two data points which are located the farthest away from the PM tube, this number changes to 38.2 ($\approx 95.2\%$ of the light yield of the whole crystal). The corresponding numbers for the second VM2000-wrapped non-tapered crystal are 38.9 and 37.6 phe/MeV ($\approx 96.6\%$ of the light yield of the whole crystal). The difference between the two crystals is 1.4%, which is not very much. However, as this study has not been done for the crystals in the array we do not know for sure if this effect is negligible. To be on the safe side though, it would be better to use a source which irradiates the crystals from the front end side for future calibrations. Alternatively, one could demand, by a coincidence arrangement, that the muons pass the relevant parts of the crystals.

An investigation was performed for the September measurement to study if the calibration could be improved. For each crystal, a new calibration factor in the range 0.80 to 1.40 of the old one was tried in order to search for a minimum in the relative energy resolution. This was done for photon energies 24.5 and 51.6 MeV. In Figure 5.8 the result of such an optimisation for the detector below the central one is shown. A second order polynomial fit yields an additional calibration factor of 1.2 to optimise the resolution. The final calibration factor for each crystal was taken as the average of the two calibration factors obtained for the low and the high energy. The new calibration factors ranged between 1.0 from 1.2 times the old factor, with six of them being in the interval of 1.0-1.1. The energy resolution was improved (from 0.0127 to 0.0126 at 18.9 MeV and from 0.074 to 0.072 at 51.6 MeV).

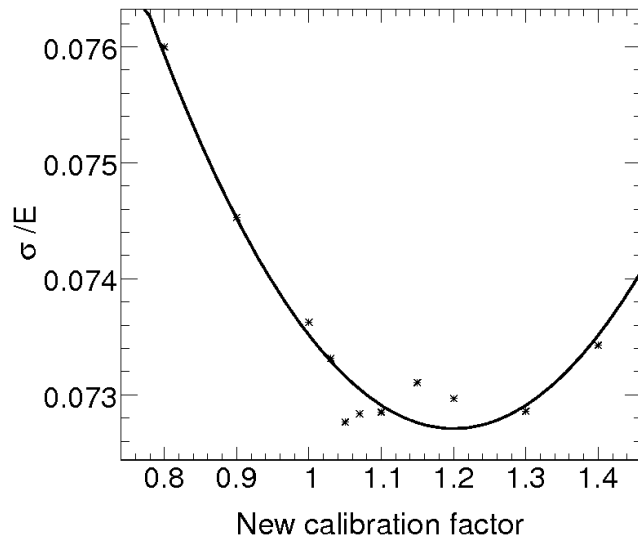


Figure 5.8: A second degree polynomial fitted to energy resolution versus the new calibration factor for one of the eight surrounding crystals at an incoming photon energy of 51.6 MeV. The new calibration factor describes how much the old calibration factor for this specific crystal should change to give the lowest energy resolution.

5.6 Results from Measurements below 60 MeV, April 2007

The 61 working taggers corresponded to photon energies ranging from 19.0 to 55.6 MeV. The relative calibration was performed and the contributions from the nine crystals were added as described in section 5.4 and the resulting energy peaks were fitted with Gaussian distributions as shown in Figure 5.9.

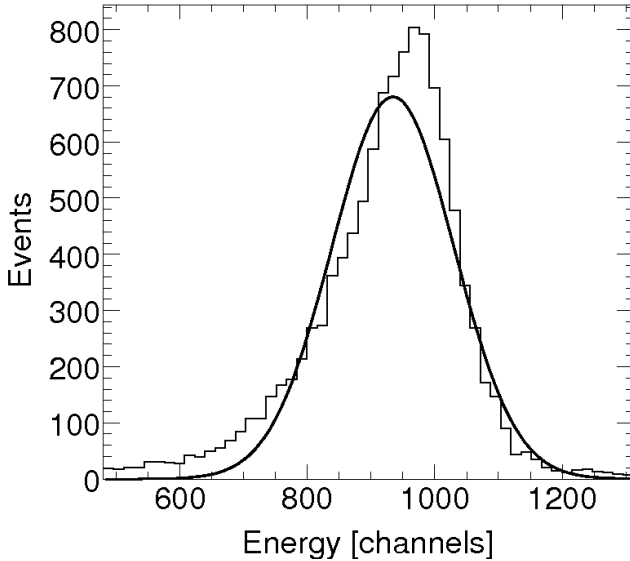


Figure 5.9: A typical summed event spectrum for an incoming photon energy $E_\gamma=35$ MeV, from the run in April. A Gaussian distribution (full drawn line) was fitted to the data.

The Gaussian distribution was used to give a simple description of the system. As the fit is not perfect, one may imagine two contributions (one from the signal and one from the leakage out of the crystal array) to the peak shape. The signal information was obtained from fitting the region corresponding to half of the height of the left hand side and the full right hand side of the peak. The relative energy resolution σ/E decreases with 16% for $E_\gamma=21.0$ MeV and with 19% for $E_\gamma=53.0$ MeV when doing this.

In Figure 5.10 the fitted peak position are shown as a function of the incoming photon energy. As expected, there is a clear linear dependence.

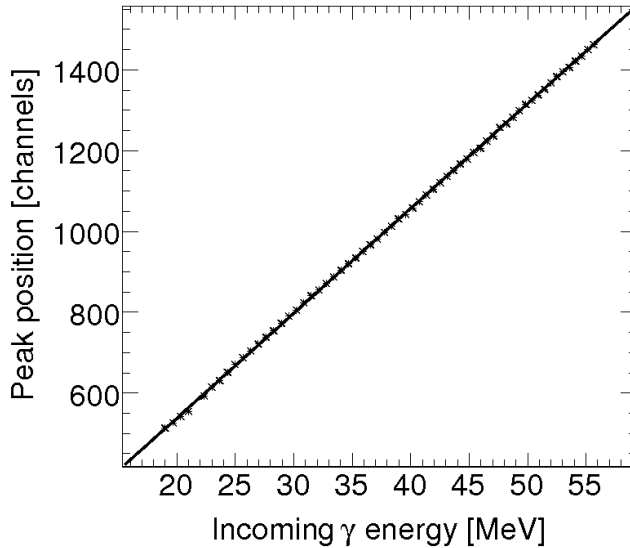


Figure 5.10: The channel number for the Gaussian centroids as a function of incoming photon energy. A straight line fit is also shown, peak position = $19.6 + 25.9[MeV^{-1}] \cdot E_\gamma$. The $\chi^2/d.o.f.$ of the fit is 11.7.

To obtain the energy resolution, the mean value of the fitted Gaussian distribution of the summed energy peak was assumed to correspond to the incoming tagged photon energy. The width (σ) was given by the fit. The relative resolution, σ/E , as a function of the incoming photon energy is shown in Figure 5.11. The value E was taken from the tagged photon energy and assumed to correspond to the mean value of the Gaussian distribution. A full drawn line fitted to the data is also shown in the same figure. The function describing the data is

$$\frac{\sigma}{E} = \sqrt{\frac{a^2}{E} + \frac{b^2}{E^2} + c^2} \quad (5.1)$$

where the parameters a^2 , b^2 and c^2 are determined by minimising the χ^2 -value of the fit. The reason for using this fit function instead of one where a , b and c are fitted, is that forcing the square of the parameters to positive puts a to zero.

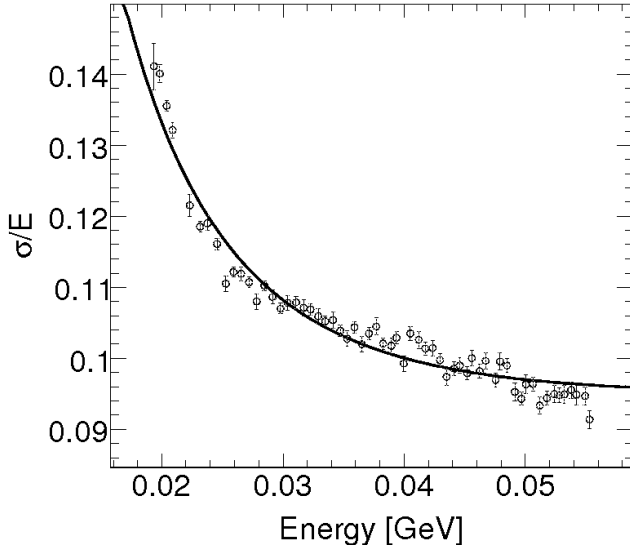


Figure 5.11: The measured relative energy resolution (open circles) as a function of tagged photon energy. The full drawn line marks the fit of the standard energy resolution expression in Equation 4.20. The value for the square of the a -parameter becomes negative and therefore all parameters from the fit are presented squared in Table 5.1. The $\chi^2/d.o.f.$ of the fit is 5.09.

	Value
$a^2 [GeV]$	$(-1.64 \pm 0.24) \cdot 10^{-4}$
$b^2 [GeV^2]$	$(6.30 \pm 0.38) \cdot 10^{-6}$
c^2	$(1.016 \pm 0.036) \cdot 10^{-2}$

Table 5.1: Squared values for the parameters a , b and c , taken from the fit in Figure 5.11.

The covariance matrix for this fit is:

$$COV_{April} = \begin{pmatrix} 5.7 \cdot 10^{-10} & -8.9 \cdot 10^{-12} & -8.4 \cdot 10^{-9} \\ -8.9 \cdot 10^{-12} & 1.4 \cdot 10^{-13} & 1.3 \cdot 10^{-10} \\ -8.4 \cdot 10^{-9} & 1.3 \cdot 10^{-10} & 1.3 \cdot 10^{-7} \end{pmatrix}$$

The correlations between parameters are calculated according to Equation 5.2,

$$\text{corr}_{xy} = \frac{COV(X, Y)}{\sigma_X \sigma_Y} \quad (5.2)$$

where X and Y denote the parameters in question. Inserting numbers gives the correlations that are presented in Table 5.2. Very large correlations (or anti-correlations) between the parameters are observed. The conclusion is that the three parameters cannot be independently determined by fitting in this limited energy interval.

One can easily understand that the imaginary value given for the a -parameter which should describe the Poisson statistics, is not reasonable as it does not have

	Correlation
$\text{corr}_{a^2 b^2}$	-0.99
$\text{corr}_{a^2 c^2}$	-0.99
$\text{corr}_{b^2 c^2}$	0.96

Table 5.2: Correlations between the squared energy resolution fit parameters for the April measurement.

a physical interpretation. Considering that we know the approximate value of this parameter from previous measurements (the number of emitted photo electrons should be close to 50 per MeV at this temperature and about 30 per MeV at room temperature [28]), the value of a can be calculated according. At $E=1$ GeV the number of photo electrons N is:

$$N = 50000 = \left(\frac{E}{\sigma_{E, \text{Poisson}}} \right)^2 = \left(\frac{1}{a} \right)^2 E \quad (5.3)$$

The value for a becomes $1/\sqrt{50000} \sqrt{\text{GeV}}$. With this input, the other two parameters can be fitted again. The resulting fit can be seen in Figure 5.12.

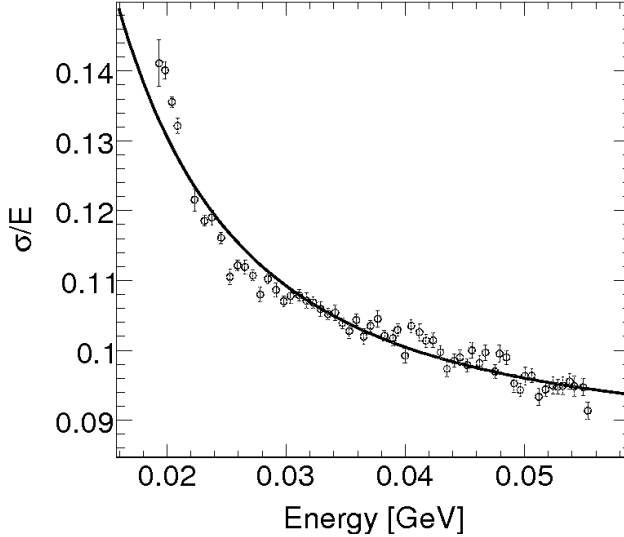


Figure 5.12: The fit to the measured relative energy resolution (open circles) as the a parameter has been given a fixed value corresponding to 50 phe/MeV. The fit parameters are presented in Table 5.3. The $\chi^2/\text{d.o.f.}$ of the fit is 6.02.

The covariance matrix for this fit is:

$$COV_{\text{April}, \text{fixed}} = \begin{pmatrix} 2.8 \cdot 10^{-15} & -2.3 \cdot 10^{-12} \\ -2.3 \cdot 10^{-12} & 2.6 \cdot 10^{-9} \end{pmatrix}$$

giving a correlation between the two fitted parameters of -0.86.

Value	
b [GeV]	$(1.85 \pm 0.23) \cdot 10^{-3}$
c	$(8.63 \pm 0.72) \cdot 10^{-2}$

Table 5.3: Values for the parameters b and c , taken from the fit in Figure 5.12. a has been fixed to $1/\sqrt{50000} \sqrt{\text{GeV}}$.

5.7 Results from Measurements below 60 MeV, September 2007

The tagged photon energies for this measurement ranged from 18.9 to 51.6 MeV. Only 47 tagged energies were used as the high amplification resulted in overflow for the highest energies. The summed energy peaks were fitted with Gaussian distributions to obtain the mean value of the peak and the σ , in order to calculate the energy resolution. When using the timing information, the σ of the fitted Gaussian distribution decreases at the same time as the mean value increases, compared to when not using this information. The change in σ/E for $E_\gamma=35$ MeV is 6.8%.

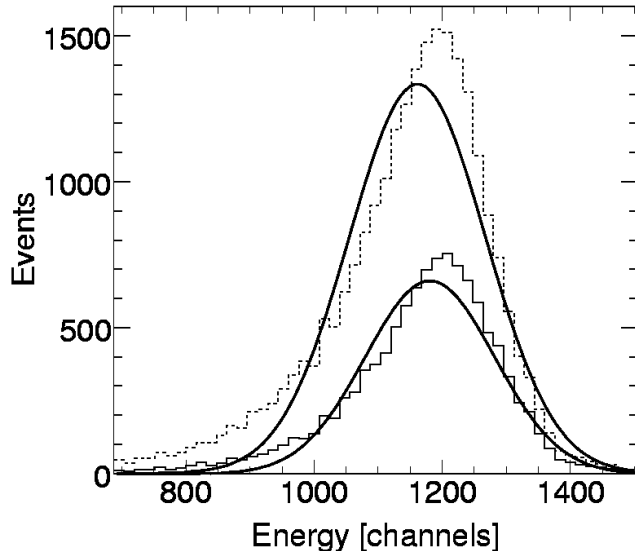


Figure 5.13: A typical event summed spectrum for an incoming photon energy of $E_\gamma=35$ MeV from the run in September. The full drawn peak is obtained when the TDC-information is used, while the dashed curve corresponds to the peak one gets without using this information.

If only half of the left hand side of the peak is fitted, the relative energy resolution σ/E decreases with 18.0% for both $E_\gamma=21.0$ MeV and $E_\gamma=49.0$ MeV.

By plotting the peak positions from the fit of the summed energy peaks as a function of the incoming photon energies, one can see a clear linear dependence, see Figure 5.14. The reason for the large $\chi^2/\text{d.o.f.}$ value is that the errors in

peak position taken from the fit are very small.

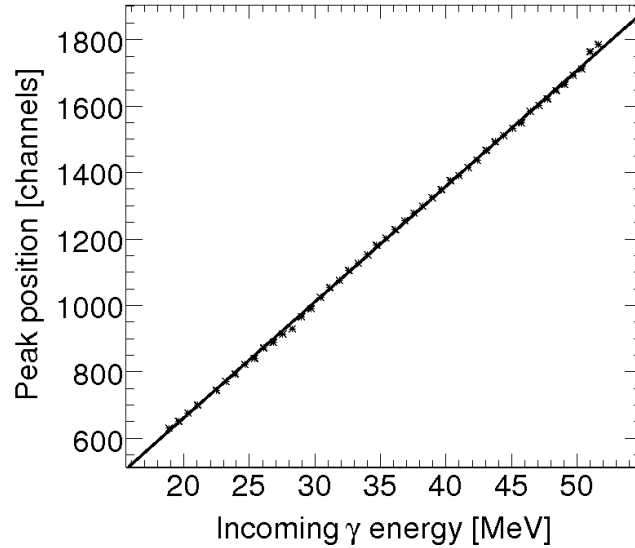


Figure 5.14: Centroid channel number for the Gaussian distributions as a function of incoming photon energy. The straight line fit is described by peak position = $-35.1 + 34.9[MeV^{-1}] \cdot E_{\gamma}$. The $\chi^2/d.o.f.$ of the fit is 20.5.

As for the April measurement, the mean values of the fitted Gaussian distributions were taken to correspond to the incoming photon energies, and the widths of the peaks were given by the fit. The relative energy resolution, σ/E , as a function of the incoming photon energy can be seen in Figure 5.15 together with a full drawn line, showing the fit of Equation 5.1.

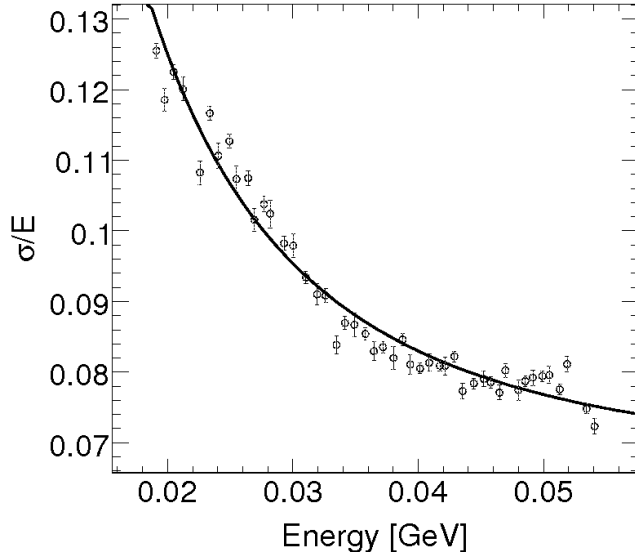


Figure 5.15: The measured energy resolution of the September data. As the fit gives a negative value for the square of the Poisson parameter a , all three fit parameters are presented squared in Table 5.4. The $\chi^2/\text{d.o.f.}$ of the fit is 6.69.

	Value
a^2 [GeV]	$(-3.1 \pm 2.4) \cdot 10^{-5}$
b^2 [GeV 2]	$(5.07 \pm 0.38) \cdot 10^{-6}$
c^2	$(4.45 \pm 0.35) \cdot 10^{-3}$

Table 5.4: Values for the square of the parameters a , b and c , obtained from the fit in Figure 5.15. The energy resolution is expressed as $\sigma/E = a/\sqrt{E} \oplus b/E \oplus c$.

Again, large correlations are obtained in the fit, cf. Table 5.5.

	Correlation
$\text{corr}_{a^2 b^2}$	-0.99
$\text{corr}_{a^2 c^2}$	-0.99
$\text{corr}_{b^2 c^2}$	0.96

Table 5.5: The correlations between the squared parameters a , b and c obtained from the fitted September data.

Because of the negative a -parameter obtained from the fit, it would again be interesting to fix its value to something reasonable and look at the new fit. a was set to correspond to 50 phe/MeV, like for the April measurements, and a new fit was performed. The result is seen in Figure 5.16.

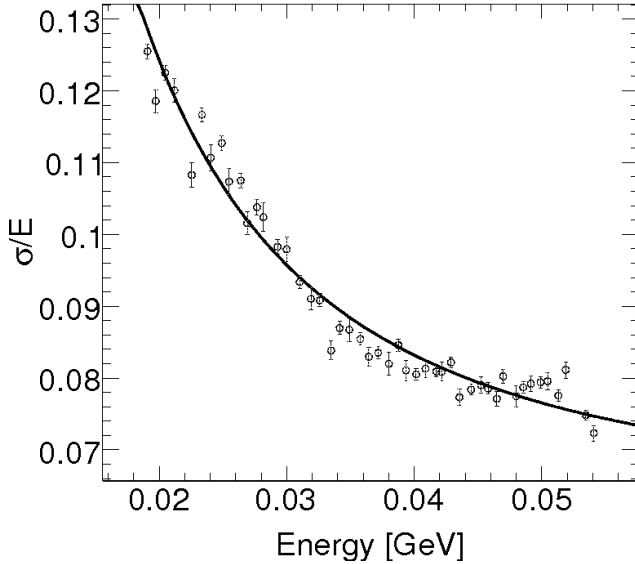


Figure 5.16: A fit to the measured relative energy resolution (open circles) with the a parameter fixed to a value that corresponds to 50 emitted phe/MeV. The fit parameters are presented in Table 5.6. The $\chi^2/\text{d.o.f.}$ of the fit is 6.64.

The values of the parameters become

	Fitted value
b [GeV]	$(2.07 \pm 0.24) \cdot 10^{-3}$
c	$(6.12 \pm 0.69) \cdot 10^{-2}$

Table 5.6: Values for the parameters b and c , taken from the fit in Figure 5.16. a has been fixed to $1/\sqrt{50000} \sqrt{\text{GeV}}$.

The resulting correlation between the two fitted parameters is -0.84.

5.8 Comparison with Previous Data

The PANDA detector will need to cover a wide range of energies in the electromagnetic calorimeter and detecting low-energy photons will be as important as detecting high-energy ones. Here we compare the present results with results obtained for higher photon energies.

In my Master thesis¹, I presented results from similar measurements at MAMI, Mainz, with PWO crystals at energies between 64 and 715 MeV for an array of 3×3 crystals. The crystals were 15 cm long, non-tapered and cooled to -24 °C during the measurements [36]. The results from the thesis were used for a new analysis and the relative energy resolution and a fit to the data is shown in Figure 5.17.

¹Published as S. Ohlsson before my name change in 2007

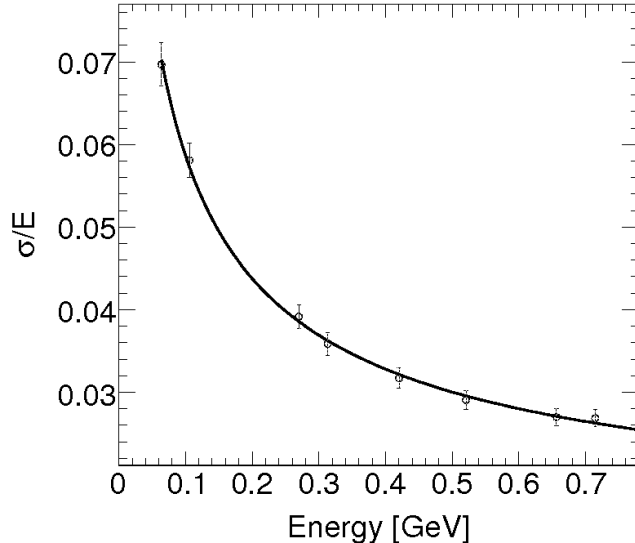


Figure 5.17: The measured relative energy (open circles) and a fit to the data (full drawn line) given in Equation 4.20. The data was taken from measurements in Mainz [36] and the fit parameters are presented in Table 5.7. The $\chi^2/\text{d.o.f.}$ of the fit is 0.21.

	Value
a^2 [GeV]	$(3.67 \pm 0.52) \cdot 10^{-4}$
b^2 [GeV 2]	$(-4.1 \pm 3.8) \cdot 10^{-6}$
c^2	$(1.84 \pm 0.93) \cdot 10^{-4}$

Table 5.7: Values for the squared parameters a , b and c , obtained from the fit in Figure 5.17. The energy resolution is expressed as $\sigma/E = a/\sqrt{E} \oplus b/E \oplus c$.

Here, the square of the b -parameter (which describes the noise contribution to the energy resolution) becomes negative but within two standard deviations consistent with the noise contribution measured in the September data ($b \approx 2$ MeV). The correlation between the parameters is somewhat smaller in this case, cf. Table 5.8.

	Correlation
$\text{corr}_{a^2b^2}$	-0.93
$\text{corr}_{a^2c^2}$	-0.94
$\text{corr}_{b^2c^2}$	0.85

Table 5.8: The correlations between the squared parameters a , b and c obtained from the fit to the Mainz data.

The parameters for the energy resolution in the interval 64 to 715 MeV are very different from those obtained from the Lund measurements. This is clearly seen in Figure 5.18 where the September data is shown together with the fit to the Mainz data. The Mainz fit predicts that the energy resolution curve should

turn downwards at low energies, in contrast to what has been measured. This feature comes from the sign of the squared b parameter.

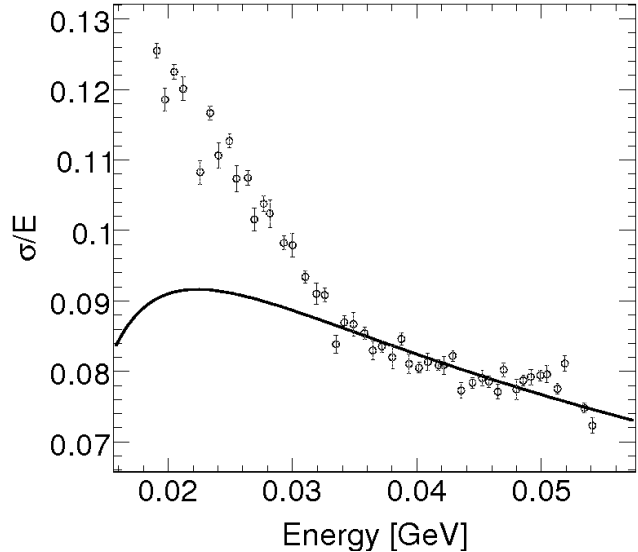


Figure 5.18: The September data points (open circles) with the Mainz fit shown with a full drawn line.

At the same time the fit to the September data does not agree with the Mainz data, cf. Figure 5.19.

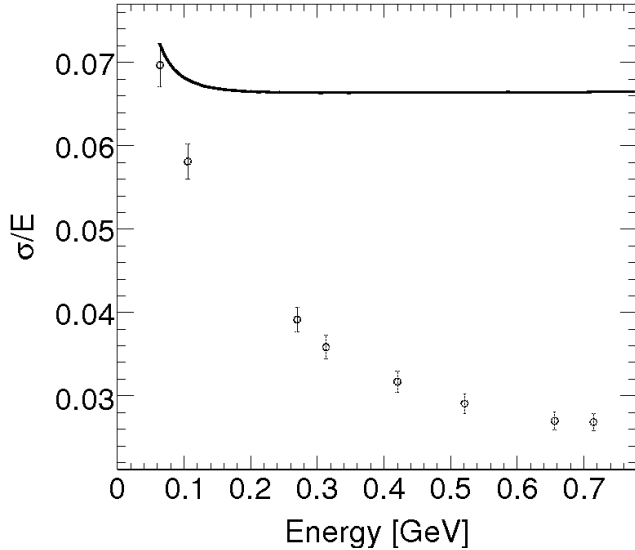


Figure 5.19: The Mainz data points are shown with open circles and the fit from the September data is shown with a full drawn line.

In Figure 5.20, the September data points are shown together with the Mainz data points. A full drawn line corresponds to the fitted energy resolution over the entire energy interval. The parameters from the fit are presented in Table 5.9.

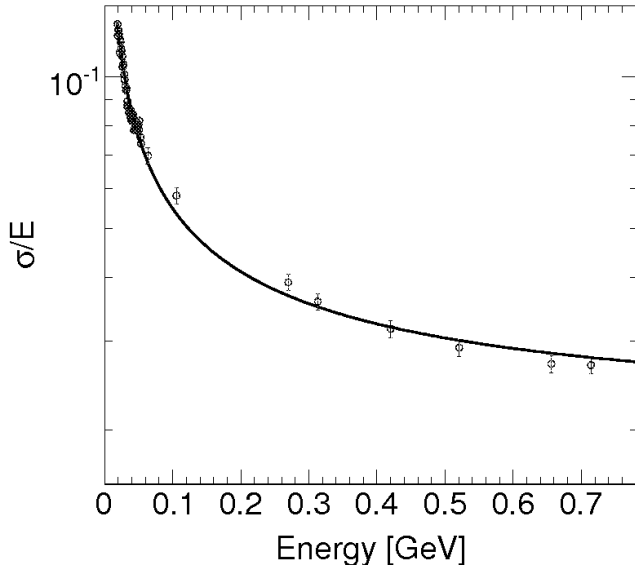


Figure 5.20: The data points from the September measurements shown together with the Mainz data points (open circles). The fit is marked with a full drawn line. The fit parameters can be found in Table 5.9. The $\chi^2/\text{d.o.f.}$ of the fit is 6.78.

	Value
$a [\sqrt{\text{GeV}}]$	$(1.55 \pm 0.21) \cdot 10^{-2}$
$b [\text{GeV}]$	$(9.50 \pm 3.3) \cdot 10^{-4}$
c	$(2.11 \pm 0.60) \cdot 10^{-2}$

Table 5.9: Values for the parameters a , b and c , obtained by fitting Equation 5.1 to the the September and the Mainz data simultaneously.

The correlations of the parameters are clearly smaller in this fit to data in a larger energy interval, cf. Table 5.10.

	Correlation
$\text{corr}_{a^2 b^2}$	-0.93
$\text{corr}_{a^2 c^2}$	-0.69
$\text{corr}_{b^2 c^2}$	0.48

Table 5.10: The correlations between the squared parameters a , b and c obtained from the fit to the combination of the September data and the Mainz data.

To understand if the values in Table 5.9 are reasonable, one can look closer at the a -parameter corresponding to the Poisson statistics from the light collection. Here, it corresponds to about 3.9 phe/MeV (at a temperature of -25°C). It is not a reasonable number. As the Poisson term a is far smaller in reality than given by the fit suggests that this term includes other effects as well. This means that the interpretation of the energy resolution terms is more difficult. The correlations between parameters are still large but they are considerable smaller between b^2 and c^2 as well as between a^2 and b^2 .

5.9 Discussion and Conclusion from the Energy Resolution Measurements

The fit to the April data as well as the September data yielded results with a negative square of the a -parameter (the Poisson parameter) in the expression for the energy resolution. If all parameters were forced to be larger than or equal to zero, the negative parameters were set to 0. That the two results gave similar results was not surprising as the measurements were in many aspects identical, except for the cooling which was better for the September measurements. The differences regarding the analysis were the optimisation of the calibration for the September measurement and the timing information that could be used to reduce the number of random coincidences. The better equipment and analysis result in a smaller relative energy resolution, σ/E , for the September data. After imposing the demand that the Poisson parameter should correspond to 50 phe/MeV, the fits became more in line with what one would expect. The fit to the eight high energy data points resulted in a squared b -parameter (the noise parameter) which was negative. The fit to the combination of the improved September data points together with Mainz data points gave however an energy resolution with only positive terms. In terms of the standard parame-

terisation (given in Equation 4.20), the statistical term appears to be reasonable, but could probably be made smaller using longer crystals (especially for high energies), less wrapping material and performing a better calibration. The small constant term c , is given by the Mainz data points which force the asymptotic value of σ/E down to approximately 0.02. However, one should keep in mind that the measurement in Mainz was different to those in Lund regarding crystal geometry and electronical set-ups.

The correlation between the three fit parameters were calculated for every energy resolution fit and very large values were obtained for both the low energies and the high energies. For the case when a fit was made to the relative energy resolutions in both the low and the high energy interval, the correlations became smaller. The values of the correlations are a clear indication of the inability to simultaneously determine the values of all three fit parameters. It means that changing the value of one parameter does not necessarily result in a different fit, since it translates into changes also in the other parameters so that a similar result can be obtained. This is clearly not desired, since each parameter should describe individual and independent contributions of both statistical fluctuations, noise and crystal properties. Due to this feature, it is not possible to discuss the energy resolution in terms of this standard expression, at least not unless the energy region over which the fit has been performed is very large.

Regarding the calibration, it was shown that using a pedestal peak and cosmic muons did not yield the best possible calibration. Lower values of σ/E were obtained by slightly adjusting the calibration constants for the eight crystals surrounding the central one. In conclusion, for future measurements it is important to ensure a good calibration. Even if the effect of the light yield uniformity of the crystals along the crystal length did not seem to play an important role here, one should use a source placed at the front end side so that the energy deposits from the source will be similar to those from the beam. Perhaps a more careful calibration can in addition lower the contribution to the energy resolution of the conventional “constant term” (which was very large for the low energy fits), or the intrinsic crystal properties. One could argue that this contribution has already been lowered in the September measurement, compared to the April measurement, by using more advanced and efficient cooling which lowers the temperature gradients inside the crystal.

From the presented figures, it is clear that the energy resolutions from the measurements in Lund and Mainz agree very well in the region around 50-70 MeV. The measured value for σ/E is 0.072 for $E_\gamma=51.6$ MeV at Lund and 0.07 for $E_\gamma=64$ MeV in Mainz. It is also evident from Figures 5.18 and 5.19, that an energy resolution parameterisation in one interval can not be applied to another energy interval. The low energy regime where the energy resolution is varying much with energy, needs to be carefully mapped since every data point gives an important contribution to describing the overall shape. Also, just fitting data points in the low energy region is not sufficient to describe the asymptotic behaviour at higher energies. The measured energy resolution at low energies is totally different from the extrapolated resolution from the Mainz data points. Also the energy resolution of the Mainz data is far better than the extrapolation of the September data suggests.

In addition, the energy resolution also depends on, for instance, the shower leakage out of the crystals, the light yield uniformity along the crystal, the absorption of light inside the crystal and developments of electromagnetic cascades

in the material before the scintillator. These contributions may have energy dependences not described by the conventional formula of Equation 4.20.

Chapter 6

Light Yield Uniformity Tests of PANDA Crystals

A very desirable feature of the calorimeter is a uniform light output from the crystals. The light sensor is located at one end and thus no position sensitivity is possible. Light yield uniformity means that, given the same energy deposition, the same number of photons should reach the light sensor, irrespectively of where they are produced. All measurements described in this section were performed at room temperature.

6.1 Set-Up for Uniformity Tests

For light yield uniformity investigations, it is of utmost importance to know where in the crystal the radiation enters. For this study, a ^{22}Na source was used. This source decays via β^+ radiation and the emitted positron very quickly annihilates with an electron from the surroundings, causing two photons, each with an energy of 511 keV, to be emitted back to back. If one uses a reasonably small scintillator to detect one of these photons and simultaneously records a signal from the main detector, the position of the incoming photon is known. This principle is shown in Figure 6.1.

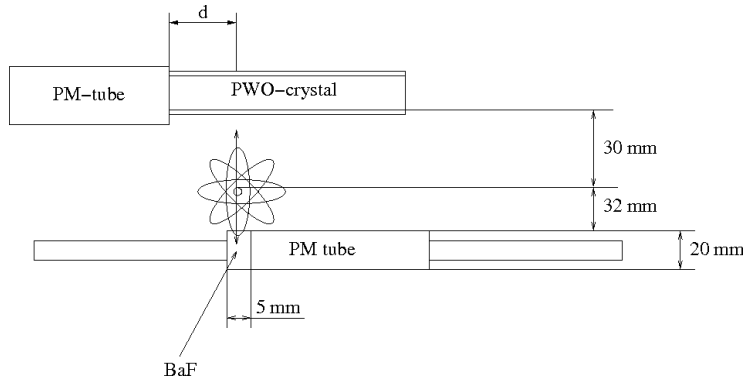


Figure 6.1: The principle of the uniformity measurements. The ^{22}Na source is located between the two scintillators and therefore it is possible to know where (distance d from the PM tube) the annihilation photons strike the PWO-crystal.

The small BaF-crystal and its PM tube were attached on a metal block which could be slid on a rod, using a handle outside the box in which the set-up was placed, see Figure 6.2.

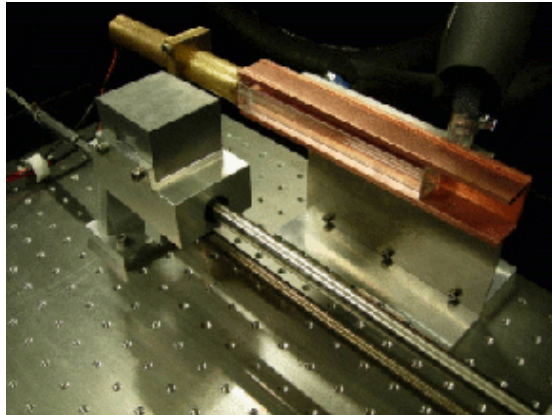


Figure 6.2: The set-up for the uniformity tests without the second scintillator and its PM tube, which were later attached where the lead collimator is located in this photograph.

Two different PWO crystal shapes were studied, three tapered and two non-tapered ones. Their dimensions are shown in Table 6.1 below.

Shape	Tapered	Non-tapered
Front-end dim. [mm ²]	28×28	20×20
Back-end dim. [mm ²]	22×22	20×20
Length [mm]	200	200

Table 6.1: The dimensions of the PWO crystals used for the uniformity measurements. The front-end is the one attached to the PM tube.

The PM tube was of the type Hamamatsu R2083 and had a diameter of 51 mm, thus fully covering the end face of the crystal. Two different wrapping materials were tried, firstly white reflective Teflon surrounded by aluminium foil and secondly VM2000 [34]. In order to understand the contribution to the light yield uniformity, the light yield was firstly investigated along the crystal. Then, the reflective properties were changed in some regions and it was studied how this affected the light yield uniformity. The electronics used for the studies were a high voltage supply, a pre-amplifier, an amplifier with a 1 μ s shaping time and a Multi Channel Analyser.

6.2 Statistics

In order to translate the measured results to the number of photo electrons emitted from the photo cathode, the energy resolution must be carefully investigated.

For a Poisson distribution with a mean value N , the standard deviation σ is given by [21]

$$\sigma = \sqrt{N} \quad (6.1)$$

Here, N is the true value of what is being measured, i.e the number of photo electrons. The pulse height S of the measured peak is proportional to the number of photo electrons produced according to $S = kN$, with k being a proportionality factor. Assuming that only the statistical fluctuations contribute to the width of the peak, the standard deviation of the pulse height σ_S , is given by $\sigma_S = k\sigma = k\sqrt{N}$.

$$\frac{\sigma_S}{S} \propto \sqrt{\frac{k\sqrt{N}}{kN}} = \frac{1}{\sqrt{N}} \quad (6.2)$$

and

$$N = \left(\frac{S}{\sigma_S} \right)^2. \quad (6.3)$$

k^{-1} was determined separately as the average of the number of photo electrons per channel for all measurements,

$$\frac{N}{S} = \left(\frac{S}{\sigma_S} \right)^2 / S = \frac{S}{\sigma_S^2} \quad (6.4)$$

and $N=k^{-1}S$ was used for the calculations.

The assumption that only statistical fluctuations contribute to the width of the peak is of course a very crude approximation, as the terms b and c in Equation 4.20 are put to zero. However, it can be justified by the fact that it gives a maximum Poisson width, or a lower bound for the number of photo electrons and any other contributions would just improve the situation. Also, taking other contributions into account would be very difficult, as the expression (meaning the individual contributions) for the energy resolution is not known in this low energy regime.

6.3 Analysis

Different positions along the crystals were investigated and at each one, pulse height spectra were recorded and fitted with a Gaussian function. The peak positions and widths were used to calculate the number of emitted phe/MeV.

6.4 Results

The plotted light yield as a function of the distance between the point of interaction and the PM tube for the measurements with Teflon wrapping is shown in Figure 6.3. There is a clear dependence of the light yield on the shape of the crystals. The tapered crystals deliver more light when the source is as far away from the PM tube as possible, while the non-tapered crystal light yields seem to be maximum close to the PM tube.

Using instead the mirror-like wrapping VM2000 the shapes of the non-uniformity is similar, but the light output is approximately 17% larger than with Teflon wrapping (see Figure 6.4).

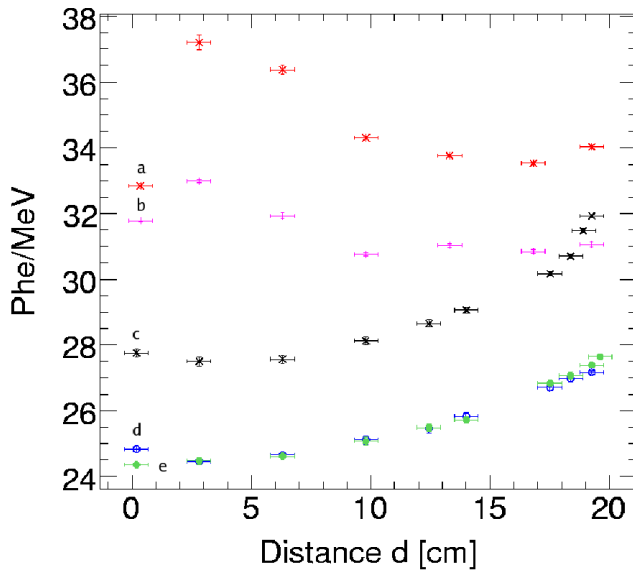


Figure 6.3: Measured light collection yield as a function of the distance d defined in Figure 6.1 for two non-tapered (a and b) and three tapered (c, d and e) PWO crystals. The crystals were wrapped with white Teflon.

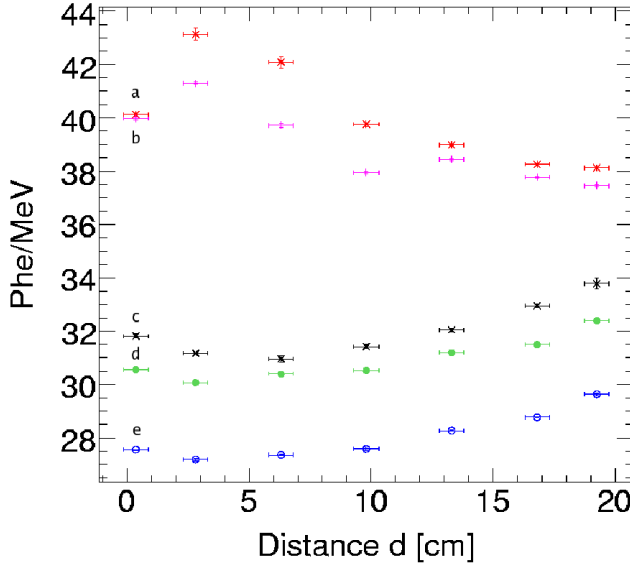


Figure 6.4: Measured light collection yield as a function of the distance d defined in Figure 6.1 for two non-tapered (a and b) and three tapered (c, d and e) PWO crystals. The crystals were wrapped with VM2000.

We quantified the uniformity by calculating, for each crystal, the ratio α_{NU} defined as:

$$\alpha_{NU} = \frac{\sqrt{\frac{1}{n-1} \sum_{i=1}^n (N_i - \bar{N})^2}}{\bar{N}} \quad (6.5)$$

where N_i is the measured number of photo electrons at the i :th interaction point and n the number of data points. This parameter describes the spread of number of phe/MeV and for a totally uniform light yield it should be 0. Using 5 data points from each crystal, α_{NU} has been calculated. To avoid end effects, the five data points were chosen correspondingly to the distances for the second to the sixth data point in the a-curve in Figure 6.3. In the cases where the exact distances were not measured, they were interpolated. The uncertainties in α_{NU} were calculated with the error propagation formula, assuming that the spread in the number of photo electrons (in Figure 6.3) was the the only uncertainty. The crystal identification information and the average value of the number of emitted phe/MeV are presented in Table 6.2, while the α_{NU} -parameters for both wrapping materials as well as the uncertainties in this value are displayed in Table 6.3.

As can be seen in Table 6.3, α_{NU} grows for the non-tapered crystals when the Teflon wrapping is substituted to VM2000, while the opposite is true for tapered crystals.

6.5 Light Yield Uniformity Improvements

Attempts to investigate the possibilities to make the light yield more uniform were done using one tapered crystal (crystal label 28_Left, seen in Figure 6.4

PWO	Crystal label	N_{Teflon}	N_{VM}
a	20_016	35.035	40.44
b	20_017	31.51	39.035
c	27_Left	28.44	31.71
d	26_Left	25.24	27.84
e	28_Left	25.23	30.74

Table 6.2: Number of photo electrons per MeV, N , averaged over the point of interaction for each of the five crystals and for the two wrapping materials. Crystal a and b are non-tapered, c-e are tapered.

PWO	α_{NU} (Teflon)	α_{NU} (VM2000)
a	$(4.718 \pm 0.041) \cdot 10^{-2}$	$(5.152 \pm 0.046) \cdot 10^{-2}$
b	$(3.017 \pm 0.067) \cdot 10^{-2}$	$(3.787 \pm 0.045) \cdot 10^{-2}$
c	$(3.73 \pm 0.23) \cdot 10^{-2}$	$(2.55 \pm 0.20) \cdot 10^{-2}$
d	$(3.21 \pm 0.38) \cdot 10^{-2}$	$(2.395 \pm 0.041) \cdot 10^{-2}$
e	$(3.23 \pm 0.31) \cdot 10^{-2}$	$(1.92 \pm 0.20) \cdot 10^{-2}$

Table 6.3: he measured non-uniformity, α_{NU} , for each of the five crystals and for the two wrapping materials.

as data set e). In order to investigate the importance of photon reflections at different parts of the crystal surface, four different ways were tried. They were: 1) no reflective wrapping on the crystal side opposite of the PM tube, 2) black tape (1 cm wide) put 2 cm from the end of the crystal, 3) black tape (2 cm wide) put 2 cm from the end of the crystal and finally 4) two stripes of 2 cm wide tape put at two opposite sides of the crystal about 2 cm from the end side, cf. Figure 6.5.



Figure 6.5: The location of the tape for the study of light yield uniformity improvements. The tape is put 2 cm from the end side of the crystal and it is either 1 cm or 2 cm wide. For the 2×2 cm of tape option, there is an equal amount of tape on the opposite side of the crystal.

The expectation was that without reflective wrapping on the short end of the crystal, the light would scatter out, thereby decreasing the overall light yield and perhaps affecting the shape of the non-uniformity. For using black tape, it was expected that the scattered photons would not be reflected back into the crystal, but instead be absorbed and thereby decreasing the light yield in that specific region. The results from the uniformity improvement measurements are displayed in Figure 6.6.

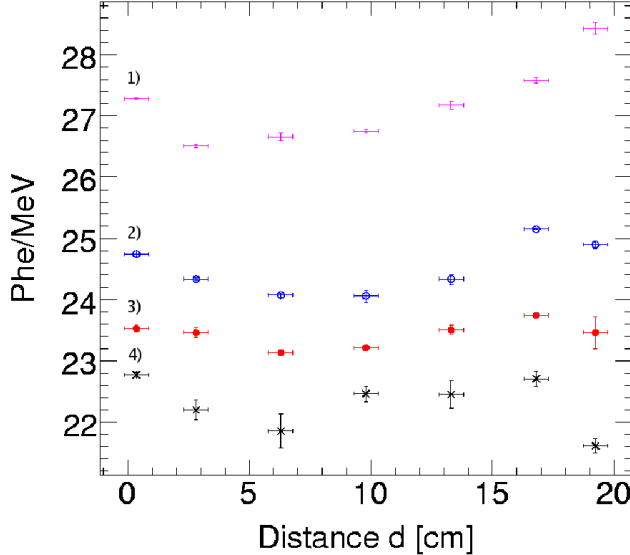


Figure 6.6: Measured light collection yield as a function of interaction point in the crystal for four different ways of making the light yield more uniform: 1) no VM2000 at the back-end, 2) 1 cm of tape, 3) 2 cm of tape and 4) 2×2 cm of tape.

α_{NU} was calculated for the four measurements and the result can be seen in Table 6.4.

Modification	Crystal label	N_{VM}	α_{NU}
Unmodified	28_Left	30.74	$(1.92 \pm 0.20) \cdot 10^{-2}$
1) Back free from VM2000	28_Left	26.94	$(1.62 \pm 0.12) \cdot 10^{-2}$
2) 1 cm tape	28_Left	24.39	$(1.828 \pm 0.052) \cdot 10^{-2}$
3) 2 cm tape	28_Left	23.41	$(1.030 \pm 0.083) \cdot 10^{-2}$
4) 2×2 cm tape	28_Left	22.33	$(1.457 \pm 0.032) \cdot 10^{-2}$

Table 6.4: The uniformity ratio α_{NU} and the average light collection yield \bar{N}_{VM} , calculated for modified VM2000 wrappings. α_{NU} for the unmodified case is included for comparison.

6.6 Discussion and Conclusions from the Uniformity Results

It is of utmost importance to keep a stable temperature while investigating the uniformity of the detector response from the PWO crystals due to the temperature dependent light yield. For these measurements, the variation in temperature was not larger than 0.1 °C. Using the dependence of the light yield on the temperature mentioned in section 4.3, the corresponding change in the light output was smaller than 0.2% and hence, the measured variation in the light collection over the crystal length (cf. Figures 6.3 and 6.4) is not a temperature effect.

As can be seen from the results in Figure 6.3 and 6.4, there are clear results that the VM2000 wrapping is superior to Teflon when it comes to reflecting scattered photons back into the crystals. Further, the light collected from the crystals is far from uniform and it also seems to be very dependent on the shape of the scintillator. From Figure 6.3 and 6.4 one can see that the overall shape of the light yield uniformity profile with the increase at large distances does not seem to depend on the wrapping material as long as the same material covers the whole crystal. According to α_{NU} , the uniformity improves when using VM2000 over Teflon for the tapered crystals, while the opposite is true for the non-tapered crystals. When tape is put on the crystals and the same non-uniformity quantity α_{NU} is calculated, it is seen that α_{NU} is decreased by a large amount. When applying 2 cm of black tape, α_{NU} is approximately 50% lower compared with the case of normal VM2000 wrapping. Even using no tape at all, but only leaving the short end opposite to the PM tube free from VM2000, lowers α_{NU} with about 15%.

Contributions to the non-uniformity for both non-tapered and tapered crystals come from light attenuation along the crystal due to intrinsic absorption inside the material, reflective properties of the crystal surface, transmission through the surface, the wrapping material as well as from diffusion on impurities and bubbles.

For the tapered crystals, the path the photons travel inside the scintillator is in general longer than for non-tapered crystals due to purely geometrical reasons. Also the number of reflections inside the crystals are larger here. Both effects increase risk of losing photons either due to internal absorption or scattering out of the scintillator thereby decreasing the number of phe/MeV.

For tapered crystals, the so-called focusing effect of the tapered shape is important. This effects favours light produced far from the PM tube (in the small end) because the reflections yield angles which are more favourable for transmitting the light into the PM tube, see Figure 6.7 [22].

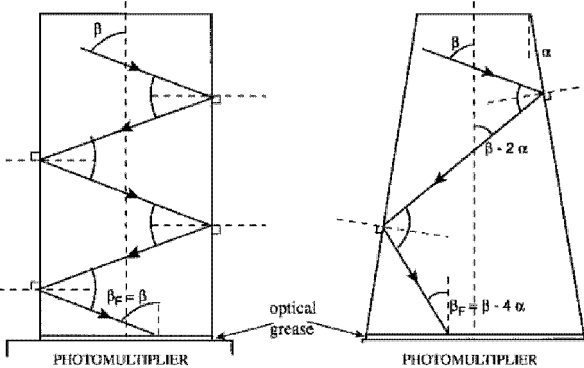


Figure 6.7: The geometrical focusing effect where the tapered geometry to the right is seen to result in more favourable angles, through which the light can escape the scintillator [22].

Total internal reflection occurs above a certain critical angle in the medium. For the PWO-to-air surface the critical angle is 25.8 degrees. At the PM tube the critical angle is increased by using an optical coupling grease. As the angles (β_F in Figure 6.7) of the photons striking the window of the PM tube are in general larger for non-tapered compared to tapered crystals, photons exit with a larger probability in the latter case. If the photon instead moves away from the PM tube with a small angle, it will for both crystal shapes suffer more reflections, but for the tapered geometry the number of reflections can grow very quickly. One should also keep in mind that it is very likely that neither wrapping material can be put close enough to the crystal so that an air gap is avoided. This air gap influences the critical angle above which total internal reflection occurs. As the difference in refraction index is larger between air and PWO than for either wrapping and PWO, this critical angle will be smaller with an air gap present and the chance for having total internal reflection and keeping the photons inside the crystal is larger. For smaller angles some photons will however escape and if there is no reflective foil beyond the air gap, these photons will disappear.

The results presented in this licenciate thesis show that the number of phe/MeV is larger for the non-tapered compared to the tapered crystals, despite the obvious geometrical disadvantages for such crystals mentioned in this section. The explanation is probably different crystal properties such as the intrinsic light yield.

It is possible to compensate for the non-uniformity of the light yield but to the cost of a decreased overall light yield. This is not an ideal solution for this type of crystal where the light yield is low to start with.

Since the electromagnetic shower occurs mainly at a depth of 4-12 X_0 into the crystal[22], one could experiment with putting tape at different positions. It is suggested that correcting for the light yield in the region 4-12 X_0 would have a critical effect while changes in the region 12-25 X_0 only would effect late developing showers[22]. Corrections in the region 0-4 X_0 would not affect the non-uniformity profile very much.

According to [22], diffuse wrappings like TYVEK and Millipore seem to give

higher light yields than Teflon does for PWO crystals, but a comparison with VM2000 was not made. It would be interesting to compare the results from such wrappings with the ones used in the investigations described here. Since the NU profile of the light yield is not affected by the different wrapping materials as long as the same type of wrapping is used for the entire crystal, these studies can be made independently of each other.

Chapter 7

Simulation Studies

7.1 Introduction

The challenging physics program of PANDA and the complexity of the detector require that substantial effort is devoted to simulations of the physics channels of interest to the collaboration. One of these topics concerns hyperon physics. The Λ particle is the lightest of the hyperons and it also frequently occurs as a decay product from excited hyperons, often together with photons (detected in the calorimeter). This makes it an obvious starting point for simulations of hyperon channels.

High quality data for the $\bar{p}p \rightarrow \bar{\Lambda}\Lambda$ reaction up to momenta of 2 GeV/c exist from the PS185 experiment at LEAR, CERN. These data can serve as a benchmark for simulations of the same reaction for PANDA.

7.2 About the Λ State

All ground state hyperons, described as baryons with strange quarks, decay only via the weak interaction, except for the Σ^0 which decays electromagnetically. Because of this, the life times for hyperons are reasonably long. For example, a produced Λ has an average flight path of several centimetres ($c\tau=7.89$ cm [1]). This typically means that the decay point is located inside, or in the vicinity of, the MVD-detector for PANDA.

Parity is not conserved in weak decays. Because of this, an asymmetry in the directions of the decay particles may be observed. If so, one can measure the hyperon polarisation, and in case of anti-hyperon-hyperon pairs also spin correlations [8].

If viewing the proton and the Λ in the constituent quark model, one can group u- and d-quarks inside the proton and the Λ into an isospin and spin zero di-quark state and let the remaining u- and s-quarks reflect the spin and isospin properties of the particles.

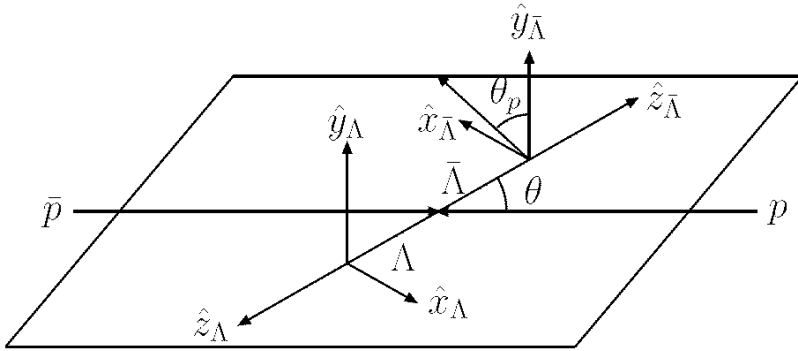


Figure 7.1: The center-of-mass frame for the $\bar{p}p$ collision, in which the coordinate systems for the rest frames of the Λ and $\bar{\Lambda}$ are shown. These coordinate systems are different for each event.

7.3 The Coordinate System

The center of mass system for the $\bar{p}p \rightarrow \bar{\Lambda}\Lambda$ is shown in Figure 7.1. In addition, we define a coordinate system for the decay particles in the rest frame of the anti-hyperon/hyperon. Here, the z-axis is given by the direction of the outgoing Λ ($\bar{\Lambda}$). The y-axis points in a direction perpendicular to the scattering plane of the $\bar{p}p$ -system and the outgoing hyperons, and the x-axis is chosen such that the system is right-handed. Formally, the axis are defined as [8]:

$$\hat{x} = \hat{y} \times \hat{z} \quad (7.1)$$

$$\hat{y} = \frac{\bar{k}_i \times \bar{k}_j}{|\bar{k}_i \times \bar{k}_j|} = \hat{n} \quad (7.2)$$

$$\hat{z} = \hat{k}_j \quad (7.3)$$

where the \bar{k}_i is the momentum vector of the initial beam. Together with the momentum vector of the outgoing hyperon, k_j , they define the interaction plane and \hat{n} is the normal vector to this plane. The index j refers to either the Λ or the $\bar{\Lambda}$ particle. As can be seen, the axis perpendicular to the interaction plane, \hat{y} or \hat{n} , is the same for the two particles.

7.4 The Angular Distributions of the Λ

The PS185 experiment collected data on the cross-sections for $\bar{p}p$ going to different single strangeness hyperon states up to a maximum \bar{p} -momentum of 2 GeV/c. Of special interest to our simulations is the reconstruction of the differential cross-sections for the Λ , in the reaction $\bar{p}p \rightarrow \bar{\Lambda}\Lambda$, and the polarisation as a function of the scattering angle in the center of mass (CM) system.

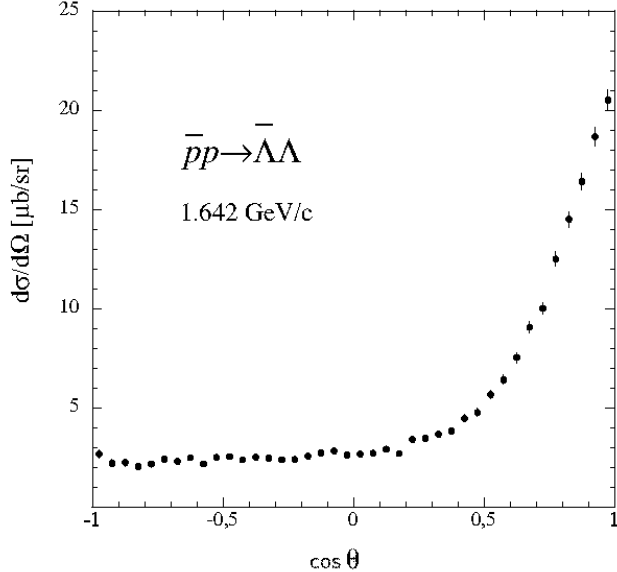


Figure 7.2: The CM differential cross-section measured by PS185 for the $\bar{\Lambda}$ in $\bar{p}p \rightarrow \bar{\Lambda}\Lambda$ reaction at the beam momentum 1.642 GeV/c [37].

To fully describe the distribution over the angular interval [38], Legendre polynomials of up to degree eight, multiplied with energy dependent coefficients $A_n(\epsilon)$ expanded in third order polynomials of ϵ , were used [39],

$$f(\cos \theta) = A_0(\epsilon) (P_0(\cos \theta) + A_1(\epsilon)P_1(\cos \theta) + \dots + A_8(\epsilon)P_8(\cos \theta)). \quad (7.4)$$

The general expression for the orthogonal Legendre polynomials $P_n(x)$ is [40]

$$P_n(x) = \frac{1}{2^n n!} \frac{d^n}{dx^n} (x^2 - 1)^n. \quad (7.5)$$

The coefficients $A_n(\epsilon)$ are polynomials depending on the excess energy ϵ

$$\epsilon = \sqrt{s} - \sum m_f = \sqrt{s} - 2m_\Lambda \quad (7.6)$$

with s being the squared total energy in the CM system. Using the four-momentum vectors p of the particles, the total energy is

$$s = (p_1 + p_2)^2 = p_1^2 - 2p_1 p_2 + p_2^2 = m_1^2 - 2p_1 p_2 + m_2^2 \quad (7.7)$$

The A_n coefficients are given by [39]

$$A_n(\epsilon) = a_{n0} + a_{n1}\epsilon + a_{n2}\epsilon^2 + a_{n3}\epsilon^3 \quad (7.8)$$

where the coefficients a_n are fitted to the experimental data. These have been implemented in the event generator for the PANDA simulations to describe the angular distributions in the hyperon energy region of PS185 (< 2 GeV/c).

7.5 Λ Polarisation

To generally describe the influence of the spin on the $\bar{p}p \rightarrow \bar{\Lambda}\Lambda$ reaction, a spin observable $\chi_{jk\mu\nu}$ can be used. It is defined as [8]

$$\chi_{jk\mu\nu} = \frac{\text{Tr}(\sigma_\mu^c \sigma_\nu^d M \sigma_j^a \sigma_k^b M^\dagger)}{\text{Tr}(MM^\dagger)} = \frac{\frac{1}{4} \text{Tr}(\sigma_\mu^c \sigma_\nu^d M \sigma_j^a \sigma_k^b M^\dagger)}{I_0} \quad (7.9)$$

where the j, k, μ and ν indices refer to the spin projection of the beam, target, scattered and recoil particles while the indices $a-d$ represent the different particles in the reaction $a+b \rightarrow c+d$. The σ matrices are the three Pauli matrices σ_1, σ_2 and σ_3 , plus the identity matrix $I_0 = \sigma_0$. M is the transition operator for $\bar{p}p$ to $\bar{\Lambda}\Lambda$. The expression is derived from a relation that describes the initial-state density matrix for spin 1/2 particles with a certain polarisation. Using expressions for the density matrices before and after interaction and the transition operator M from the $\bar{p}p$ to $\bar{\Lambda}\Lambda$, one arrives at Equation 7.9. More details on this can be found in [41].

Fortunately, the $4^4 = 256$ spin observables above can be reduced using symmetries of parity and charge conjugation and geometrical identities. The parity conservation, applied to strong interaction processes such as $\bar{p}p \rightarrow \bar{\Lambda}\Lambda$, states that the reaction probability should be unaffected by a spatial inversion of the coordinates. This gives that the polarisation of the observables in \hat{x} - and \hat{z} -directions must be zero, since they otherwise would change sign. Furthermore, charge conjugation symmetry applied to the self-conjugated $\bar{p}p$ and $\bar{\Lambda}\Lambda$ systems ensures that the polarisations for $\bar{\Lambda}$ and Λ must be equal. Finally, for polarised beam or target, invariance under rotation of the scattering plane reduces the number of spin observables additionally. These symmetries decrease the number of spin observables to the more manageable number of 40.

The Λ decays to either $p\pi^-$ or $n\pi^0$ with branching ratios of 64% and 36% respectively. In this thesis, only investigations of the charged decay mode have been done. The decay distribution for the Λ with polarisation P can be expressed as

$$I(\theta_p) = \frac{1}{4\pi} (1 + \alpha P \cos \theta_p) \quad (7.10)$$

where θ_p is the proton emission angle projected on the spin projection direction of the Λ (\hat{y} in the case of unpolarised beam and target) in the rest frame of the Λ , while α is the so-called asymmetry parameter and is related to the probability for the decay baryon to be emitted in the spin direction of the decaying hyperon. This value has been experimentally measured to be 0.64 for the Λ (-0.64 for the $\bar{\Lambda}$) [8].

7.5.1 How to Reconstruct the Λ Polarisation

The polarisation is extracted from the reconstructed data by considering the distribution of the decay particles according to Equation 7.10. The probability for a particle to fall within this distribution over the entire interval is 100%, meaning that the probability density function should be

$$A \int \frac{1}{4\pi} (1 + \alpha P \cos \theta) d\cos \theta = 1 \quad (7.11)$$

with A being a normalisation constant. Substituting $\cos \theta$ with x and performing the integration gives $A=2\pi$. Hence, the normalised distribution function becomes

$$f(x) = \frac{1}{2}(1 + \alpha Px). \quad (7.12)$$

Calculating the mean value of x according to [21] gives

$$\langle x \rangle = \int_{-1}^1 x f(x) dx = \frac{1}{2} \int_{-1}^1 (x + \alpha Px^2) dx = \frac{\alpha P}{3} \quad (7.13)$$

and substituting x with $\cos \theta$ gives the relation

$$P = \frac{3}{\alpha} \langle \cos \theta \rangle \approx \frac{3}{\alpha} \overline{\cos \theta} = \frac{3}{\alpha N} \sum_{i=1}^N \cos \theta_i \quad (7.14)$$

with N being the number of reconstructed events. To get an estimate of the uncertainty in the reconstructed polarisation, the square root of the variance is calculated according to [42]

$$\frac{3}{\alpha} V(\overline{\cos \theta}) = \left(\frac{1}{N} \right)^2 V \left(\sum_{i=1}^N \cos \theta_i \right) = \frac{3}{\alpha} \frac{1}{N} V(\cos \theta) \quad (7.15)$$

where $V(\cos \theta)$ is the estimated value for the variance of the polarisation distribution

$$V(\cos \theta) = \frac{1}{N-1} \sum_{i=1}^N (\cos \theta_i - \overline{\cos \theta})^2. \quad (7.16)$$

7.6 The PANDA Software Frameworks

PANDA has today two different software frameworks, one which is referred to as the BaBar-like framework and the other referred to as the PandaROOT framework. Both are C++ based software for Monte Carlo simulations, event reconstruction and physics analysis for the PANDA experiment.

The BaBar-like framework was the first one available to the collaboration and it was to a large extent inherited from the BaBar collaboration. It contains many well debugged libraries and tools and has been successfully used in the BaBar experiment for many years. It has been decided to use this framework until the PANDA physics book is completed in 2008. After that, PandaROOT will be the framework for Monte Carlo simulations and data reconstruction.

The PandaROOT framework is an object-oriented ROOT-based framework inspired by the CMS collaboration. It is fully based on the use of C++ class libraries from the ROOT data analysis framework [35]. ROOT is a widely used software package in nuclear and particle physics and thus has a large community of developers which the PANDA community can profit from. Through the use of ROOT, the PandaROOT framework implements the concept of Virtual Monte Carlo (VMC) [43]. VMC is a set of library classes which enables the user to implement a particle physics detector simulation without beforehand defining the particle transport code, such as Geant3[44], Geant4[45] or Fluka[46], to be used.

7.7 Reconstruction

7.7.1 Generation of Particles

Events for the simulations have been produced by a modified generator which was originally used at the PS185 experiment at LEAR. As of now, it is an integrated part of the software framework and the information on the differential cross-sections for $\bar{p}p \rightarrow \bar{\Lambda}\Lambda$ production has, as well as polarisation and spin correlations, been added.

The generator makes a call to the CERNLIB routine FOWL which then returns the momentum vectors for the generated $\bar{\Lambda}\Lambda$ in the CM system, according to a isotropic distribution. This distribution is then adapted to the experimental differential cross section shown in Figure 7.1. The selection process is done by keeping $\Lambda(\bar{\Lambda})$ -events with a probability given by the value of the angular distribution for this certain $\cos\theta$, divided by the maximum value of the angular distribution.

The momentum of the generated anti-protons has been set to 1.64 GeV/c as this was one of the energies used also for the PS185 experiment. The beam spread is set to 0.01%. The interaction point is set to (0, 0, 0), with a smearing in x- and y-direction according to a Gaussian distribution centred around zero and with a standard deviation of 1 mm, given by the pellet target. The smearing in the z-direction is confined to a circular region with a radius of 1 mm. The branching fraction of $\Lambda \rightarrow p\pi^-$ as well as the polarisation have been set to 100%. The transport code used for the p, \bar{p} , π^+ and π^- to simulate the interactions with the detector materials is Geant4.

The sub-detectors used for the reconstruction is the MVD, the STT, the two MDCs (each having 8 layers) in the target spectrometer and the six MDCs (each having 6 layers) in the forward spectrometer [23]. 198 000 pairs of $\bar{\Lambda}\Lambda$ were generated.

7.7.2 Angular Distribution

The reconstructed distribution for $\cos\theta$ for the $\bar{\Lambda}$ in the CM frame together with the Monte Carlo truth for those events are shown in Figure 7.3. There is an excellent agreement between the two curves.

The $c\tau$ of the $\bar{\Lambda}$ was also simulated and reconstructed. The result can be seen in Figure 7.4. For the reconstructed events, $c\tau=7.419\pm0.029$ cm, while the Monte Carlo truth of those events gives $c\tau=7.396\pm0.029$ cm. The Monte Carlo truth of all generated $\bar{\Lambda}$ yields a decay length of 7.862 ± 0.018 cm. The established experimental value is 7.89 cm [1]. It should be investigated why there is a 5 mm bias on the decay length of the $\bar{\Lambda}$.

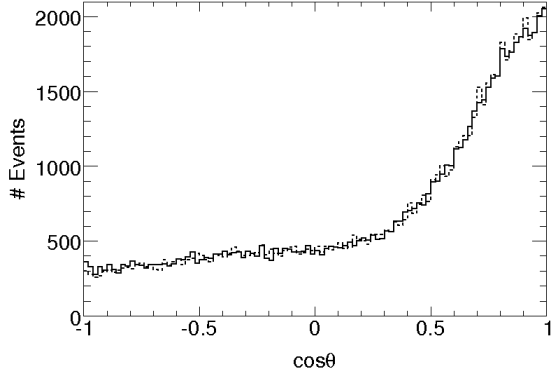


Figure 7.3: The reconstructed $\cos \theta$ distribution for the $\bar{\Lambda}$ is shown with a full drawn line and the Monte Carlo truth for those particles with a dashed line.

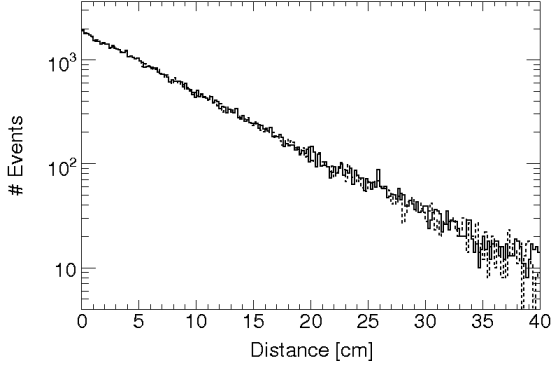


Figure 7.4: The reconstructed $c\tau$ of the simulated $\bar{\Lambda}$ is shown with a full drawn line and the Monte Carlo truth of those events with a dashed line.

7.7.3 Detector and Detection Efficiency

We define the *detection efficiency* by the ratio of the number of reconstructed events to the number of generated particles. Out of the 198 000 generated $\bar{\Lambda}\Lambda$ pairs, 70 267 are reconstructed, translating into roughly 35%.

The *detector efficiency* reflects the ability of the detector to correctly detect particles over the angular interval. From reconstructed unpolarised Λ and $\bar{\Lambda}$ particles, one can investigate the $\cos \theta_p$ distributions of the daughter proton and anti-proton in x-, y- and z directions defined earlier over the interval (-1, 1) in the $\bar{\Lambda}$ rest frame. For full detector efficiency, these plots should be isotropic if there is no polarisation in any direction. However, this is not the case, as can be seen in Figure 7.5.

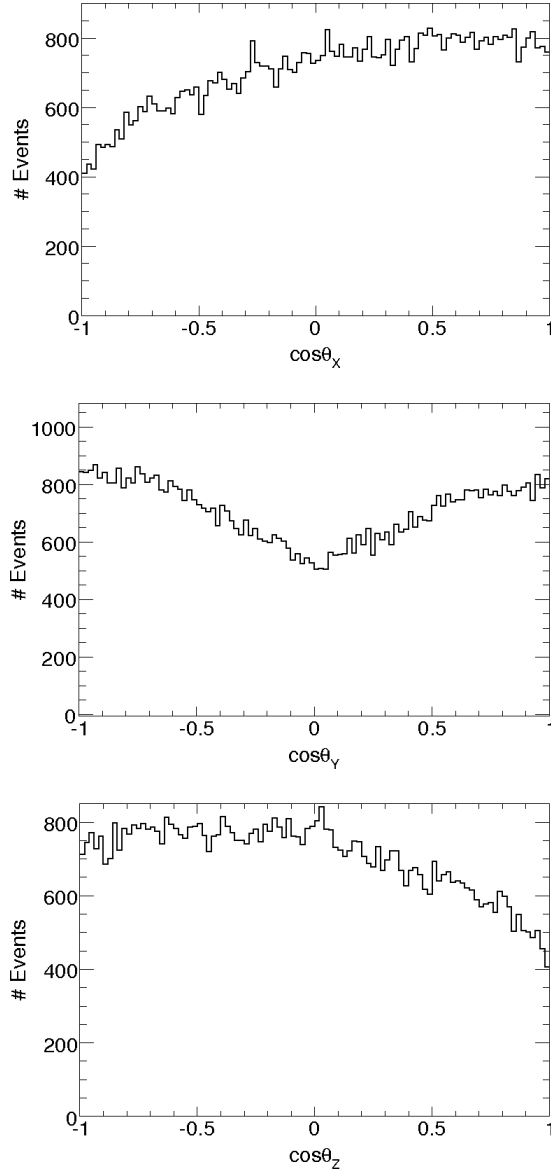


Figure 7.5: Reconstructed distributions for $\cos\theta_{\bar{p}}$ for the decay anti-proton with respect to the x-axis 7.5(a), y-axis 7.5(b) and z-axis 7.5(c) in Figure 7.1 for unpolarised $\bar{\Lambda}$ particles.

There is a lack of anti-protons in the backward x-direction in Figure 7.5(a) and there are anti-protons missing in the $\cos\theta_y = 0$ region of Figure 7.5(b), meaning perpendicular to the y-axis. For the outgoing $\bar{\Lambda}$, the x-axis tends to point in the backward direction of the laboratory system (in the direction of the negative z-values rather than the positive), as can be seen in Figure 7.1, even if it varies with every event.

The missing anti-protons in Figure 7.5(a) indicate that the corresponding missing π^+ will go in the direction of $\cos\theta_x$ being close to 1, meaning backwards

in the laboratory system. In the same way, from Figure 7.5(b) one understands that the missing π^+ may go either along the positive x-axis or in the direction of the negative z-axis. In cases when the pions do go in these directions, they will become slow because of the strong forward boost due to the incoming anti-protons. If so, one would expect a dip in the region of $\cos \theta$ approaching +1 in Figure 7.5(c) and this is exactly what is seen.

The corresponding distributions of reconstructed $\cos \theta_{\bar{p}}$ (see Figure 7.1) in the case of polarised $\bar{\Lambda}$ is seen in Figure 7.6.

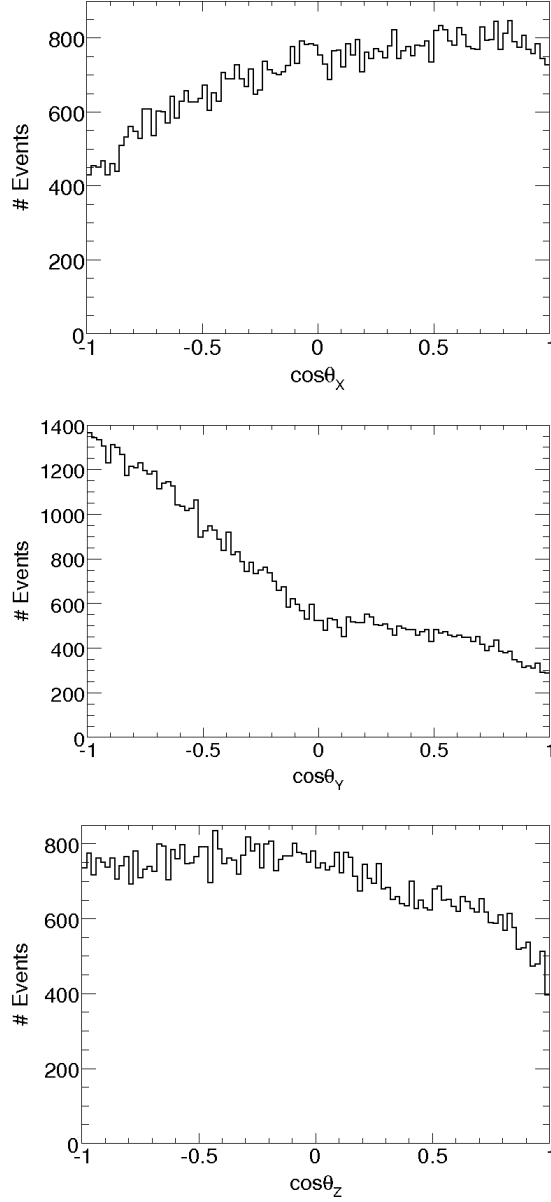


Figure 7.6: Reconstructed distributions for $\cos \theta$ for the daughter anti-proton with respect to the x-axis 7.5(a), y-axis 7.5(b) and z-axis 7.5(c) for polarised $\bar{\Lambda}$ particles.

In Figure 7.6(a) and Figure 7.6(c) one would once again expect a flat distribution and for Figure 7.6(b) a slope corresponding to the polarisation times the asymmetry parameter $\alpha/2$. However, one notices a lack of particles in the same regions as in Figure 7.5.

To further investigate the detector response in different angular regions of the detector, one can plot the polarisation as a function of $\cos \theta_{\bar{\Lambda}}$ in the CM system. For an isotropic detector response, one would expect a constant polar-

isation independent of the $\theta_{\bar{\Lambda}}$ angle as the polarisation is set to 100%. As can be seen in Figure 7.7, this is not quite the case.

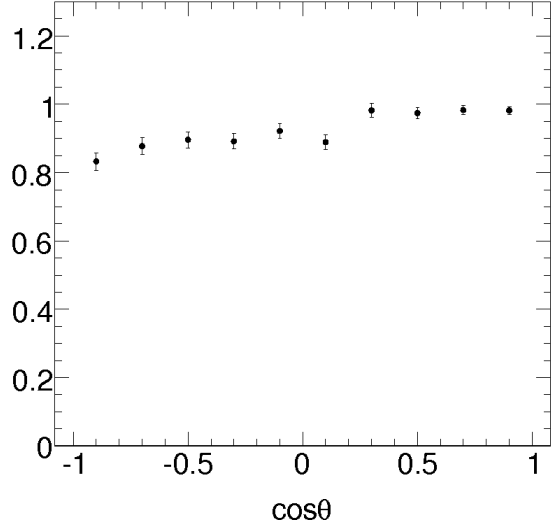


Figure 7.7: The calculated polarisation as a function of $\cos \theta_{\bar{\Lambda}}$ in the CM system.

The reason why the distribution is not constant over the entire angular is not known and should be investigated further.

Slow Pions

For a correct reconstruction of the Λ and $\bar{\Lambda}$, it is important to correctly reconstruct the decay particles - the proton and the pion. The pion is the most critical one, since its much lower mass generally causes it to be emitted with a larger velocity than the proton. If the pion goes backwards in the detector, seen in the laboratory system, it will become very slow because of the boost in the opposite direction and may even spiral in the detector due to the solenoid field, without undergoing detection. There may also be difficulties with the software regarding handling of spiralling particles, resulting in fewer pions being reconstructed.

Figures 7.8 and 7.9 show histograms of the pion momentum from the generated Monte Carlo pions as well as of the reconstructed ones. The decay pions have momenta between 0 and approximately 0.3 GeV/c. However, only pions with momentum above 0.05 GeV/c are reconstructed. Consequently, events with such slow pions will be missed in Figure 7.5 and 7.6.

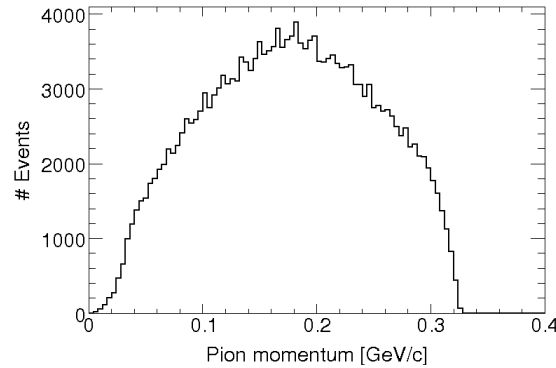


Figure 7.8: Magnitude of the π^+ momentum for the Monte Carlo truth of the generated particles.

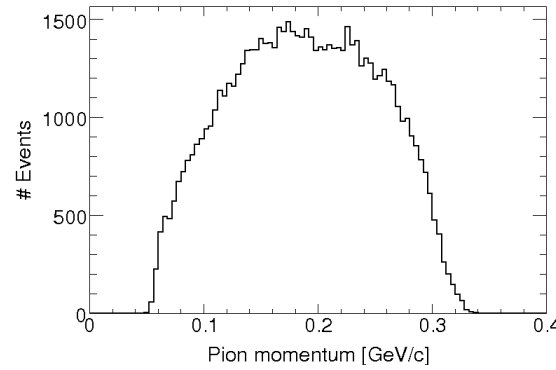
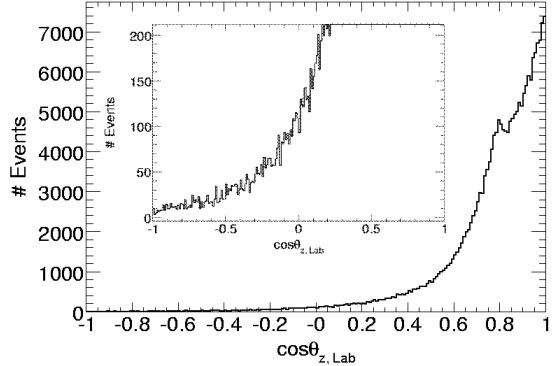
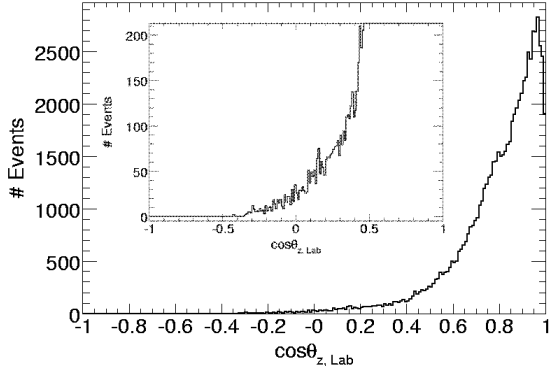


Figure 7.9: Magnitude of the π^+ momentum for the reconstructed particles.

Another way to study where the reconstruction of the pion fails is to look at the the π^+ angles in the laboratory system and compare them to the reconstructed ones. Also here, one can see that the angular distributions differ.



(a) Laboratory emission angle of the Monte Carlo π^+ .



(b) Laboratory emission angle of the reconstructed π^+ .

Figure 7.10: Angle of the Monte Carlo truth and the reconstructed π^+ in the detector. The angle $\theta_{\bar{\Lambda}}$ is measured in the laboratory system.

Zooming in in Figure 7.10(a) and 7.10(b), one can see from Figure 7.10 that pions going backward in the detector are not reconstructed, probably because they are simply too slow to undergo reconstruction in the solenoid field. This is also what was suggested in connection to figures 7.5 and 7.6. The peak close to $\cos \theta = 0.7$ in 7.10(a) comes from the case when the $\bar{\Lambda}$ goes in the direction of $\cos \theta_{\bar{\Lambda}}$ close to 1. In this case, the pion can not go backwards in the laboratory system. If it is emitted “backwards” in the $\bar{\Lambda}$ rest system, with respect to the flight direction of the $\bar{\Lambda}$ in the laboratory system, there is a maximum in its laboratory emission angle θ_{Lab} . This is what is seen.

7.7.4 The Polarisation

The polarisation and its errors were calculated using the formulae given in section 7.5.1. The results on the reconstructed polarisation are presented in the Table 7.1, while the Table 7.2 contains the average polarisation calculated from the Monte Carlo truth of the reconstructed particles. The polarisation should be 100% in y-direction and 0% in x- and z-direction.

One can see that the reconstructed polarisations agree quite well with the Monte Carlo truth for those particles, however it is far from being $(0, 1, 0)$ in the x-,

	x-direction	y-direction	z-direction
100% pol	$-0.3511 \pm 9.9 \cdot 10^{-3}$	$1.151 \pm 1.1 \cdot 10^{-2}$	$0.2546 \pm 9.9 \cdot 10^{-3}$
0% pol	$-0.3445 \pm 9.9 \cdot 10^{-3}$	$-0.066 \pm 1.1 \cdot 10^{-2}$	$0.2846 \pm 9.8 \cdot 10^{-3}$

Table 7.1: Reconstructed average polarisation for non-polarised and polarised $\bar{\Lambda}$ -particles, as well as calculated standard deviation for these values.

	x-direction	y-direction	z-direction
100% pol	$-0.3368 \pm 9.9 \cdot 10^{-3}$	$1.156 \pm 1.1 \cdot 10^{-2}$	$0.2546 \pm 9.9 \cdot 10^{-3}$
0% pol	$-0.3311 \pm 9.9 \cdot 10^{-3}$	$-0.068 \pm 1.1 \cdot 10^{-2}$	$0.2944 \pm 9.8 \cdot 10^{-3}$

Table 7.2: Polarisation of the Monte Carlo truth of the reconstructed particles in the cases of no and full polarisation, respectively. The calculated standard deviation for these values are also shown.

y- and z-directions. The polarisation even takes on unphysical values of having a magnitude larger than 1. Taking the statistical uncertainties into account does not reduce the discrepancy between the generated and reconstructed events enough, and the reason must therefore be caused by the detector response and reconstruction inefficiencies.

The polarisations can also be extracted from the plots of the $\cos \theta$ -distributions for the decay protons, Figure 7.6. A straight line fit over the interval should have a slope of $\alpha P/2$ with P being the polarisation (here equal to 1 since it has been set to 100% in the event generator). To get a realistic measure of the polarisation, the histograms should however first be compensated for the acceptance of the detector and the reconstruction ability, Figure 7.5. Using the Monte Carlo truth of the reconstructed non-polarised $\bar{\Lambda}$ to calibrate for the acceptance and efficiency gives the result seen in Figure 7.11. The uncertainties have been calculated from the error propagation formula, using an uncertainty in each bin of the histograms proportional to the square root of the number of events in that bin.

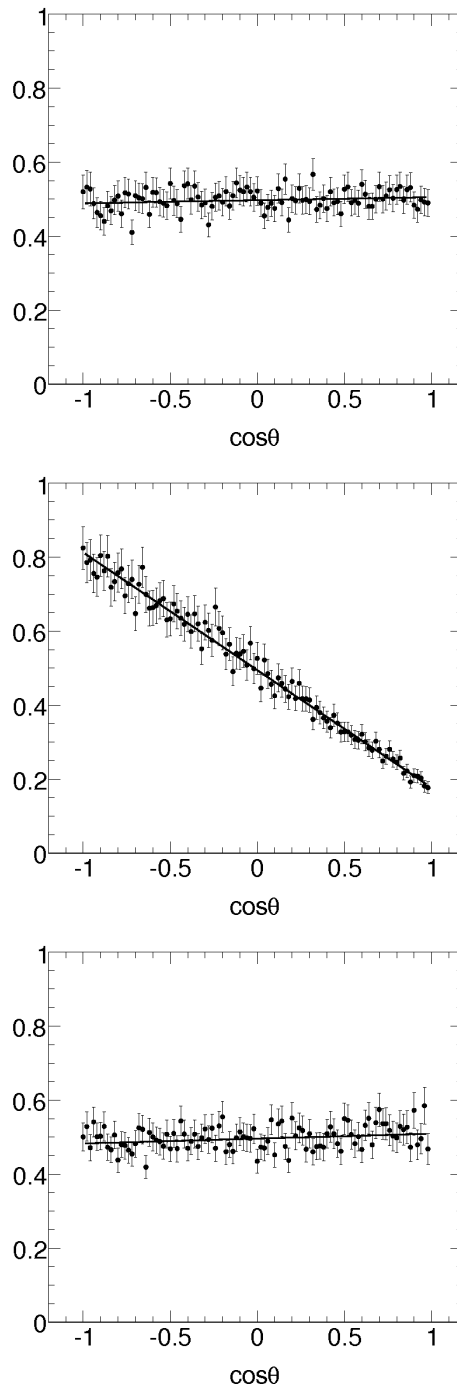


Figure 7.11: Efficiency calibrated $\cos\theta$ distributions. The slopes of the fitted functions correspond to $\alpha P/2$.

The fitted values for the slopes obtained from the three plots in Figure 7.3 are shown in Table 7.3.

Slope, x-direction	Slope, y-direction	Slope, z-direction
0.0084 ± 0.0066	-0.3175 ± 0.0058	0.0133 ± 0.0067

Table 7.3: Calculated reconstructed average polarisation for polarised Λ -particles. The values have been corrected for the detector response.

The values from the slopes should be multiplied with $2/\alpha$ to get the polarisation, due to the factor $1/2$ in Equation 7.12. Hence, one gets the polarisation multiplied with the asymmetry factor along the y-axis to be 0.63, leading to a polarisation of $(99 \pm 1.8)\%$. The polarisation along the x and the z-axis are $(2.6 \pm 2.0)\%$ and $(4.1 \pm 2.1)\%$ respectively. The values including errors are displayed in Table 7.3.

7.7.5 Momentum and Vertex Reconstruction

The momenta of the decay protons and pions must be well reconstructed to correctly describe the hyperons. This is also related to how well the decay point is reconstructed. As the previous study unveiled, the reconstruction of the slow pions must be improved. An important follow-up question is how well the reconstructed momenta of the daughter particles describe their true momenta.

In the case of a reconstructed decay $\bar{p}p$ system, the reconstructed momentum for the decay protons and pions in x-, y- and z-direction were plotted against the Monte Carlo truth for that specific event. The plots showed a very good correspondence for both pions and protons, as can be seen in Figures 7.12 and 7.13.

The differences between reconstructed and generated momenta were also plotted to display how big the deviations were. The results are presented in Figure 7.14 and 7.15 together with the root mean square (RMS) values.

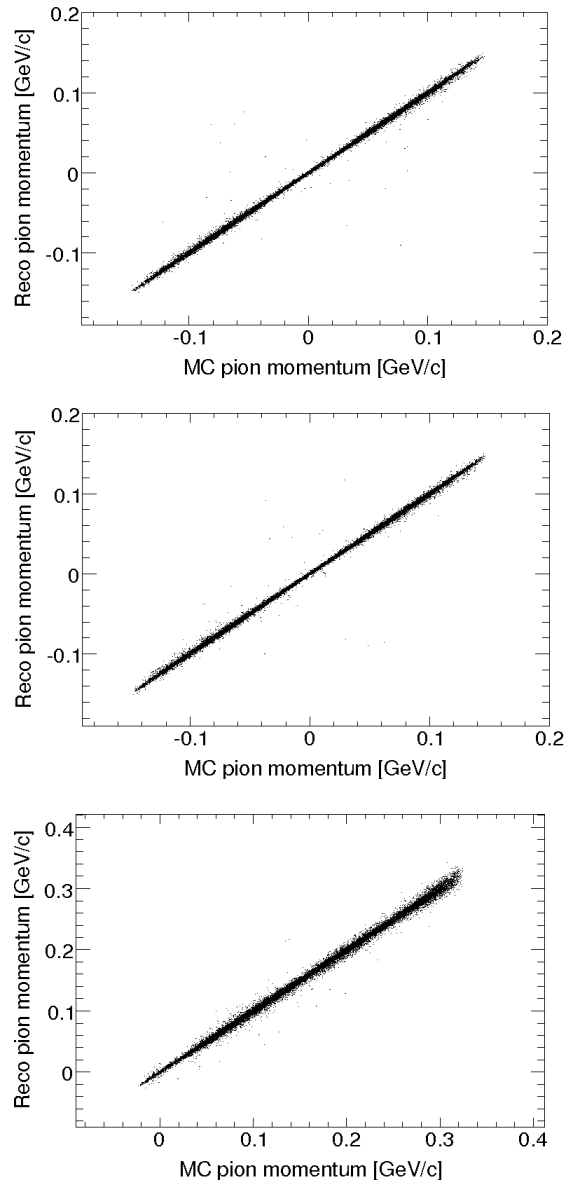


Figure 7.12: Reconstructed π^+ momenta versus Monte Carlo momenta in the x-direction 7.13(a), y-direction 7.13(b) and z-direction 7.13(c).

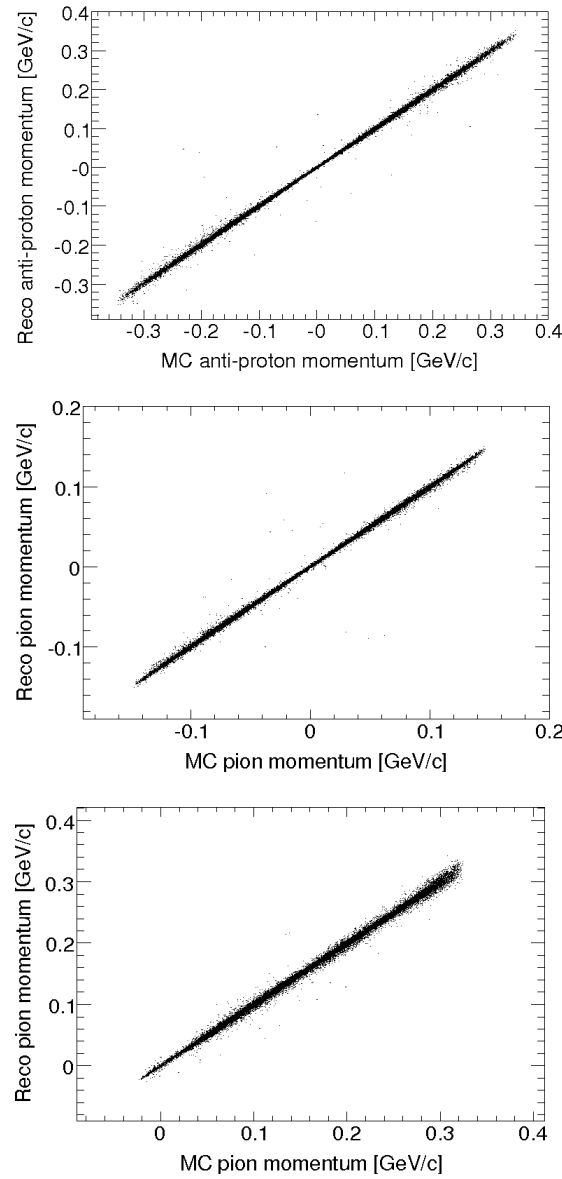


Figure 7.13: Reconstructed anti-proton momenta versus Monte Carlo momenta in the x-direction 7.12(a), y-direction 7.12(b) and z-direction 7.12(c).

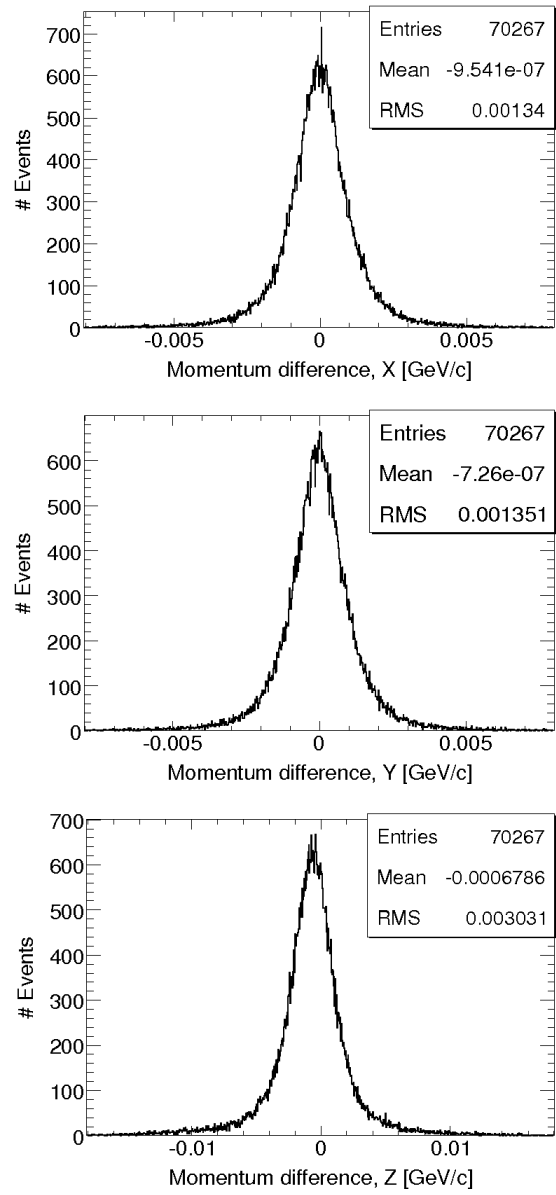


Figure 7.14: The reconstructed momenta components minus the corresponding Monte Carlo truth for the π^+ .

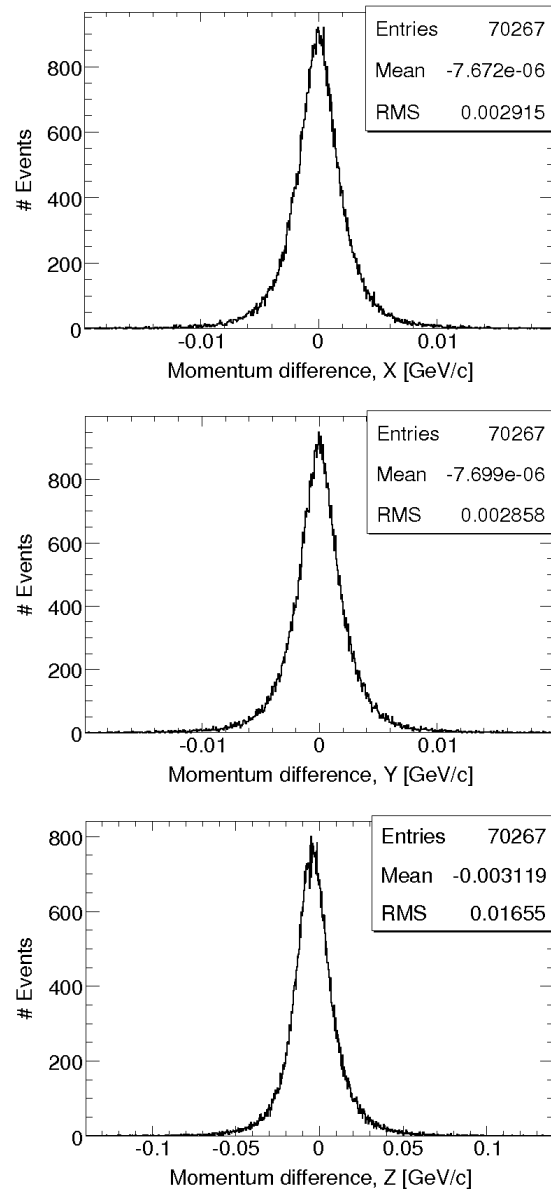


Figure 7.15: The reconstructed momenta components minus the corresponding Monte Carlo truth for the \bar{p} .

Also the reconstructed decay vertex of the $\bar{\Lambda}$ agrees well with its generated values as can be seen in Figure 7.16.

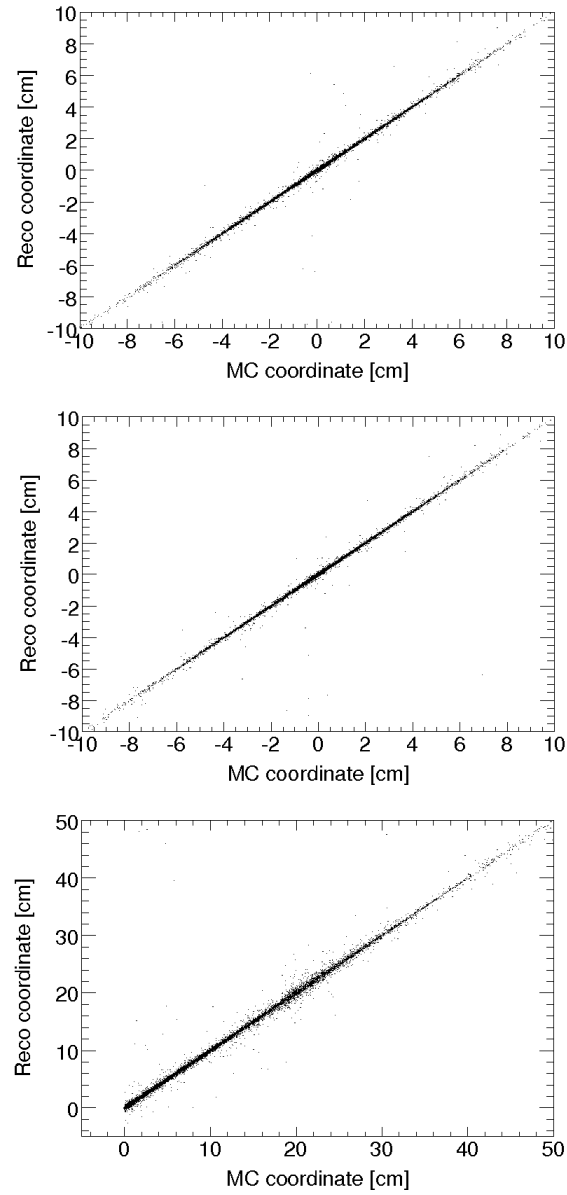


Figure 7.16: Reconstructed $\bar{\Lambda}$ decay vertex coordinates versus the Monte Carlo coordinates in the x-direction 7.16(a), y-direction 7.16(b) and z-direction 7.16(c).

The difference between the reconstructed vertex coordinates and the Monte Carlo truth is shown in Figure 7.17.

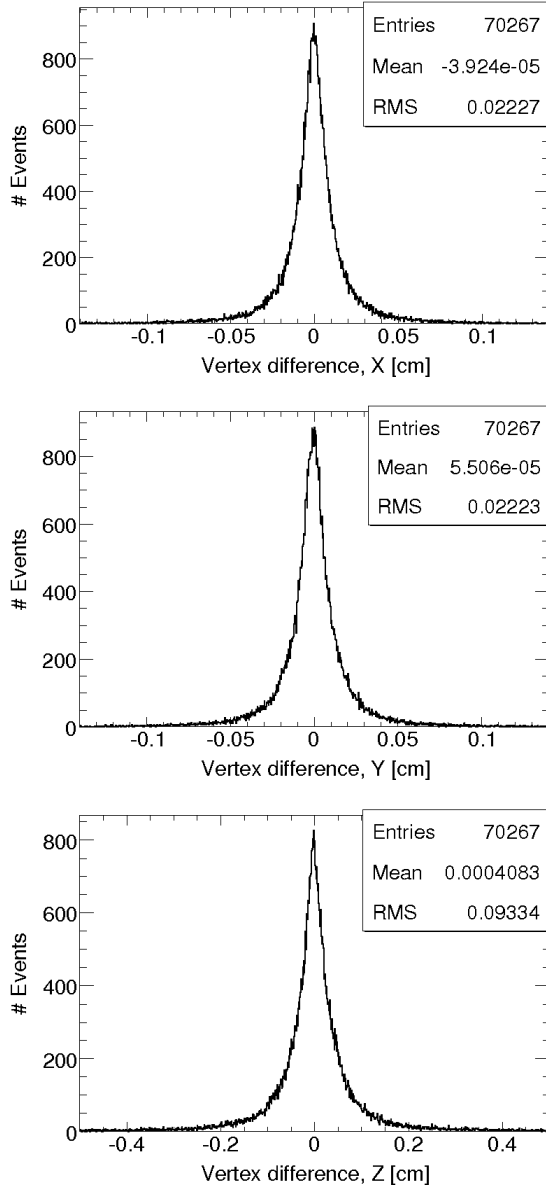


Figure 7.17: The reconstructed vertex components minus the corresponding Monte Carlo truth for the $\bar{\Lambda}$.

7.8 Conclusions from the Simulation Results

The $\bar{p}p \rightarrow \bar{\Lambda}\Lambda$ reaction is reconstructable in the BaBar-like framework of PANDA. However, there are obvious problems with reconstructing slow pions coming from the decay of the hyperons. This will affect the reconstruction of the hyperon polarisation, as can be seen in the non-isotropic distributions of $\cos \theta_p$ for the anti-protons coming from the unpolarised $\bar{\Lambda}$ particles. As a consequence, one must take the detector response into account in order to obtain the correct po-

larisation. If this is done, a polarisation similar to the Monte Carlo truth is obtained. More detailed studies are necessary to investigate how much of this is due to the detector response and the software reconstruction respectively.

In those cases when the daughter pion and proton are reconstructed, the life time and decay vertex of the decaying hyperon look very similar to the Monte Carlo truth of those events. Also the reconstructed momentum of the daughter particles correspond well to the Monte Carlo truth.

Chapter 8

Conclusion and Outlook

8.1 Conclusion

This licenciate thesis has treated the topics of energy resolution and light yield uniformity measurements of PWO crystals for PANDA, as well as software reconstruction of the $\bar{p}p \rightarrow \bar{\Lambda}\Lambda$ reaction including polarisation.

Two energy resolution measurements were done using a 3×3 array of non-tapered crystals, cooled to -15 °C and -25 °C, respectively. The tagged photon beam of energies between 19 and 56 MeV at MAX-Lab was used. The energy contributions from all nine crystals were summed and the resulting peaks were fitted with Gaussian distributions to extract the resolution. The relative energy resolution for the September measurements was 0.12 at a photon energy of 18.9 MeV 0.072 at 51.6 MeV. The measured relative energy resolution, expressed as the standard deviation σ of the Gaussian distribution divided by the photon energy E was fitted with the parametrisation $\sigma(E)/E = a/\sqrt{E} \oplus b/E \oplus c$. For both the April and the September measurement, the energy resolution expression contained a negative square of the Poisson parameter, a . This has not a physical interpretation, but might be understood in terms of the large correlations with the other two parameters. After imposing the condition that the a -parameter should correspond to a light yield of 50 phe/MeV, an energy resolution of $\sigma/E = 0.45\%/\sqrt{E_{GeV}} \oplus 0.18\%/E_{GeV} \oplus 8.63\%$ was obtained for the April measurement. For the September data the result became $\sigma/E = 0.45\%/\sqrt{E_{GeV}} \oplus 0.21\%/E_{GeV} \oplus 6.12\%$. Upon combining data points from the September measurement with eight data points for energies ranging between 64 and 715 MeV, it was seen that the energy resolutions agree very well in the overlapping range of 50-70 MeV. The fit over the entire energy interval becomes positive and is given by $\sigma/E = 1.6\%/\sqrt{E_{GeV}} \oplus 0.095\%/E_{GeV} \oplus 2.1\%$. However, there is a very large correlation (anti-correlation) between all three parameters. For the two low energy measurements at MAX-Lab, the magnitude of these correlations are close to 100%. For the combined fit, they are slightly lower between the parameters a and c as well as for b and c . It seems as the standard parameterisation is not ideal in describing the energy resolution at low energies or in explaining it in terms of something that has physical relevance.

The light uniformity measurements were performed with two non-tapered and three tapered PWO crystals and a ^{22}Na source. Two different crystal

wrappings were used: white Teflon covered with aluminium foil and mirror-like VM2000. Pulse height spectra were recorded at different source positions along the crystals and the number of photo electrons per unit energy was determined as a function of interaction point in the crystal. For the tapered crystals the light collection yield increased with the distance between the interaction point and the PM tube. For the non-tapered crystals the light collection yield peaked somewhere close to the PM tube. The shape of the responses was qualitatively the same irrespective of which wrapping was used, but using VM2000 gave a 17% higher overall light output. Black tape was put on different positions on one of the tapered crystals in an attempt to make the light yield more uniform. Placing black absorbing tape to one or two of the lateral surfaces close to the short end of the crystal decreased the increase of light yield in this region, however, at the expense of an overall decrease in light yield.

A simulation of the $\bar{p}p \rightarrow \Lambda\bar{\Lambda}$ reaction at a momentum of 1.64 GeV/c was done in the BaBar-like software Framework for PANDA. 198 000 $\Lambda\bar{\Lambda}$ pairs were created using a modified generator originally made for the PS185 experiment at LEAR, CERN. The reconstruction efficiency was found to be about 35%. The angular distribution of the $\bar{\Lambda}$ could be reconstructed correctly. Figures of the reconstructed versus Monte Carlo momenta of the decay pion and anti-proton agree well, as does the vertex position of the decaying hyperon. It was discovered that slow pions are difficult to reconstruct as they tend to spiral in the solenoid field of the detector without being seen by the sub-detectors. At 100% polarisation perpendicular to the scattering plane and without compensating for the angular detector efficiency, the reconstructed polarisation of the $\bar{\Lambda}$ does not reproduce the correct value in the direction of the true polarisation (\hat{y}) and is significantly different from 0 in the direction of the outgoing hyperon (\hat{z}) and as well along the third axis (\hat{x}). By correcting data with the results from unpolarised events, a polarisation which is $(2.6 \pm 2.0)\%$, $(99 \pm 1.8)\%$ and $(4.1 \pm 2.1)\%$ along \hat{x} , \hat{y} and \hat{z} , respectively, is obtained.

8.2 Outlook

The next step in energy resolution measurements with PANDA PWO crystals is to use a 5×5 array of tapered crystals shaped for the forward end-cap and cool it to -25 °C to repeat the measurements described in this thesis. This will ensure that the electromagnetic showers are contained inside the crystal array, and a better energy resolution is expected.

Regarding the light yield uniformity measurements, it would be interesting to develop a masking technique for improved uniformity than just placing arbitrary amounts of tape on different sides of the crystals. It is important to develop a technique which is applicable for larger amounts of crystals and which does not require individual adaptations for each crystal.

For the simulations of the hyperons the next step is to repeat the same steps at higher momenta of the incoming anti-protons and to investigate the influence from background reactions, such as elastic scattering and $\bar{p}p \rightarrow \bar{p}p\pi^+\pi^-$. Hyperon channels with photons among the end products, such as Σ^0 and $\Lambda(1405)$, will later also be studied to connect the hyperon channels with the electromagnetic calorimeter.

Acknowledgement

Firstly I would like to thank my two supervisors professor Tord Johansson at the Department for Physics and Astronomy in Uppsala and professor Per-Erik Tegnér at the Department of Physics at Stockholms University for their time, support and useful comments. They have both contributed with valuable ideas on how to make this work meaningful. Tord Johansson has been very helpful in pointing out areas of interest in the hyperon field and in putting the different parts of this thesis together. I am also very happy about the hands-on help I have received from Per-Erik Tegnér during all sorts of crystal measurements as well as the patience he has shown me when it has been time to discuss the analysis.

Further, I would like to thank the staff at MAX-Lab in Lund for making things run smoothly during the crystal measurements; Bent Schröder, Kurt Hansen, Paweł Golubev, Lennart Isaksson and the accelerator crew. A special thanks goes out to Lennart Isaksson for helping me sort out access to all the data. Also in connection to this, I would like to thank Linda Karlsson for keeping such good track of the temperature during the April measurements and the two visiting students Jan Schulze and Jörn Becker for great company in Lund as well as for help with the electronical set-up.

I would also like to direct a “thank you” to the Bochum group in the PANDA collaboration for being helpful when it comes to generating files for the simulations. Especially, Jan Zhong deserves a big medal for being more than helpful at all times of both the day and the year.

Another thanks goes out to my office mate Erik Thomé and his long lasting patience and for reading this thesis at an early stage. Thanks for contributing with good company and interesting discussions on anything and everything at all times. Even though you may not always seem to have very strong opinions on different topics, I know you can surprise.

Finally I would like to thank Oscar Stål who also found the time to read through this thesis and comment on it, as well as anyone else who has contributed to this work by putting up with my occasional bad moods, cheered me up or helped me formulate tricky paragraphs. Or all three of them.

Thanks to all my colleagues at the department for a pleasant working environment and for help with providing or solving cross words during the coffee breaks! Even if you most likely blame me when things go wrong in the latter case...

Bibliography

- [1] Particle Data Group, *Journal of Physics G: Nuclear and Particle Physics*, Institute of Physics Publishing, 2006
- [2] B.R. Martin and G. Shaw, *Particle Physics*, John Wiley and Sons, West Sussex, England, 2003
- [3] FAIR Baseline Technical Design Report. Technical Report, FAIR/GSI, Darmstadt, 2006.
<http://www.gsi.de/documents/DOC-2006-Jul-40-1.pdf>
- [4] R. Novotny, *Fast and Compact Lead Tungstate-Based Electromagnetic Calorimeter for the PANDA Detector at GSI*, IEEE
- [5] R.K. Ellis and W.J. Stirling and B.R. Weber, *QCD and Collider Physics*, Cambridge University Press, United Kingdom, 1996 transaction on nuclear science, vol. 51, no 6, Dec. 2004
- [6] A. Lundborg, *The Charm of Excited Glue*. PhD thesis, Uppsala University, February 2007
- [7] S. Godfrey, *The XYZ's of c anti-c: Hints of exotic new mesons*, Proceeding of 4th Flavor Physics and CP Violation Conference (FPCP 2006), Vancouver, British Columbia, Canada, 9-12 Apr 2006, pp015, arXiv:hep-ph/0605152.
- [8] T. Johansson, *Antibaryon-baryon production in antiproton-proton collisions*. Proceedings of the international school of physics «Enrico Fermi», Societá Italiana di Fisica, 2004
- [9] The PANDA Collaboration. *Technical Progress Report for PANDA. Strong Interaction Studies with PANDA*. Technical report, FAIR/GSI, February 2005.
- [10] J. Eschke, *International Facility for Antiproton and Ion research Facility (FAIR) at GSI, Darmstadt*, J. Phys. G: Nucl. Part. Phys. 31 (2005) S967-S973
- [11] Homepage of GSI: <http://www.gsi.de/> 26-10-2007
- [12] FAIR Joint Core Team, *FAIR Facility for Antiproton nd Ion Research*. Technical Report, FAIR/GSI, October 2007.

- [13] The PANDA Collaboration. GSI Conceptual Design Report *An Accelerator Facility for Beams of Ions and Antiprotons*. Technical report, FAIR/GSI, November 2001.
- [14] L. Schmitt, Presentation given at the Swedish FAIR Consortium Meeting in Gothenburg, Sweden, 2007-11-12, *The PANDA experiment*.
- [15] U. Lynen et al., *Simulation of the Straw Tube Tracker for the PANDA Detector*
[www.gsi.de/informationen/wti/library/scientificreport2002/files/207.pdf=2007-11-09](http://www.gsi.de/informationen/wti/library/scientificreport2002/files/207.pdf)
- [16] The PANDA Collaboration. *Forward End Cap of the PANDA EM Calorimeter, Mechanical Design Report*. Technical Report, June 2007.
- [17] K.S. Krane, *Introductory nuclear physics*, John Wiley and Sons, 1988
- [18] S. Bergenius Gavler, *Counting Calories - Studies of Energy Loss in a Segmented Calorimeter*. PhD thesis, KTH, April 2006
- [19] F. Mandl and G. Shaw, *Quantum Field Theory*, John Wiley and Sons, England, 2006
- [20] W.R. Leo, *Techniques for Nuclear and Particle Physics Experiments*, Springer-Verlag, Berlin Heidelberg, 1994
- [21] P.R. Bevington and D.K. Robinson, *Data Reduction and Error Analysis for the Physical Sciences*, McGraw-Hill, New-York, 2003
- [22] E. Auffrey, et al., *Crystal conditioning for high-energy physics detectors*. Nucl. Instr. and Meth. A 486 (2002) 22-34
- [23] Jan Zhong. Private communication.
- [24] A. Golischewski, *Simulationsbasierte Studien der Reaktion $\bar{p}p \rightarrow \eta_c \rightarrow \gamma\gamma$ zur Optimierung des PANDA-Detektors*, Diploma Thesis, Bochum-Ruhr University, Juni 2005
- [25] T. Thörnlund, Department of Nuclear and Particle Physics, Uppsala University
- [26] L. Rappe, *Quantum Computing with naturally trapped sub-nanometre-spaced ions*. PhD thesis, Lund University, 2006.
- [27] B. Lewandowski, et al., *Scintillation crystal development: Irradiation and light response to hadrons*, Proposal to the KVI Program Advisory Committee, Exp. No. T18, October, 2003.
- [28] L. Karlsson, *Investigating The Light Collection From Lead Tungstate (PWO) Scintillators at Low Temperatures*, Master Thesis at Stockholm University. To be published.
- [29] H. Löchner, *Scintillation detectors for radiation hard electromagnetic calorimeters*, presentation at Calor2004
http://calor.pg.infn.it/calor2004/pres/tuesday_morning/loehner.pdf

- [30] MAX-Lab Homepage: <http://www.maxlab.lu.se/maxlab/index.html> 26-10-2007
- [31] J-O. Adler, et al., *The photon tagging facility at the MAX accelerator system in Lund*, Nucl. Instr. and Meth. A 294 (1990) 15-25
- [32] *MAXLAB, användarhandbok* 2006-10-02
www.maxlab.lu.se/user-info/safetyinstr_sw.pdf 2007-11-08
- [33] J-O. Adler, *The new nuclear physics beam line at MAB-lab*, 5th Workshop on “e-m induced two hadron emission”, 2001.
- [34] R. Novotny. Private communication.
- [35] The ROOT System Homepage: <http://root.cern.ch/> 26-10-2007
- [36] S. Ohlsson, *Test and Developments of Crystals for a High-Resolution Electromagnetic Calorimeter for PANDA*, Master thesis, Uppsala University, June, 2004.
- [37] P.D. Barnes, et al., *Observables in high-statistics measurements of the reaction $\bar{p}p \rightarrow \bar{\Lambda}\Lambda$* , Phys. Rev. C, vol. 54, no4, (1996), p 1877.
- [38] G. Arfken and H. Weber, *Mathematical methods for physicists*, Harcourt/Academic Press, 2001
- [39] T. Johansson. Private communication.
- [40] L. Råde and B. Westergren, *Mathematics Handbook for Science and Engineering*, Studentlitteratur, Lund, 1998
- [41] K. D. Paschke, et al., *Experimental determination of the complete spin structure for $\bar{p}p \rightarrow \bar{\Lambda}\Lambda$ at $p_{\bar{p}}=1.637$ GeV/c*, arXiv:nucl-ex/0605025 v1, May, 2006
- [42] A.G. Frodalen and O. Skjeggestad, *Probability and statistics in particle physics*, Universitetsforlaget, Norway, 1979
- [43] Virtual Monte Carlo at ROOT: <http://root.cern.ch/root/vmc/>
- [44] GEANT - Detector description and simulation tool, CERN Program Library Long Write-up W5013, CERN, Geneva, 1993,
<http://wwwasdoc.web.cern.ch/wwwasdoc/pdfdir/geant.pdf> 26-10-2007
- [45] Geant4 Homepage: <http://geant4.web.cern.ch/geant4/> 26-10-2007
- [46] Fluka Homepage: <http://www.fluka.org/> 26-10-2007